약학박사학위논문

# DNA 나노구조 기반 약물 전달 연구
## DNA nanostructure-based systems
## for drug and nucleic acid delivery

2015 년 8 월

서울대학교 대학원
약학과 약제과학전공
김 미 경

# Abstract

## DNA nanostructure-based systems
## for drug and nucleic acid delivery

Mi-Gyeong Kim

Physical Pharmacy, Department of Pharmacy

The Graduate School

Seoul National University

Rolling circle amplification (RCA)-based DNA nanotechnologies have attracted tremendous interest to develop new platform of drug delivery. First, DNA nanoballs with antisense oligonucleotide (ASO)-complementary sequences could provide sequence-specific loading of dual ASOs, Dz13 and OGX-427, and coating with hyaluronic acid (HA) promoted CD44 receptor-mediated delivery of ASOs to tumor cells. Importantly, ASOs delivered by HA-coated DNA nanoballs silenced the expression of their target mRNAs of ASO, exerting potent anticancer effects in vitro and in vivo. Second, DNA polyaptamer nanothreads of protein tyrosine kinase 7 (PTK7) receptor were synthesized by RCA. To enhance the anchoring capability of polyaptamers onto reduced graphene oxide (rGO), oligonucleotide bridge sequence between repeating aptamer sequences was introduced. Surface

modification of rGO with DNA polyaptamer nanothreads (PNTrGO) resulted in improved cellular uptake into PTK7-positive tumor cell lines and enhanced tumor tissue accumulation compared to oligoT-bridged scrambled polyaptamer-anchored rGO nanosheets. Moreover, systemic administration of doxorubicin using PNTrGO enhanced the antitumor effects in mice bearing PTK7-positive tumors. Third, an injectable hydrogel based on drug-specific DNA polyaptamer networks was developed by using graphene oxide (GO) nanosheets as a crosslinker. Graphene oxide-crosslinked DNA polyaptamer (GO-PA) hybrid hydrogels were constructed by running single step RCA of DNA template in the presence of GO nanosheet. GO-PA hybrid hydrogel showed drug-specificity towards kanamycin. The drug loading efficiency of GO-PA was 58.0 % for kanamycin, but 1.2% for gentamicin.

**Keywords:** DNA nanostructures, rolling circle amplification, drug delivery, aptamer, graphene oxide, reduced graphene oxide

# Contents

# List of Tables

# List of Figures

# List of Abbreviations

| Abbreviation | Word |
|---|---|
| **ARP** | ASO-hybridized RCA product |
| **ASOs** | antisense oligonucleotides |
| **ANOVA** | analysis of variance |
| **CCK-8** | cell counting kit-8 |
| **Cy5.5** | cyanine 5.5 dye |
| **DAPI** | 4',6-diamidino-2-phenylindole dihydrochloride |
| **Dox** | doxorubicin |
| ***E. coli*** | *Enterobacteriaceae coli* |
| **FAM** | fluorescein |
| **F-Kan** | fluorescent kanamycin |
| **F-Gen** | fluorescent gentamicin |
| **Gen** | gentamicin |
| **GO** | graphene oxide |
| **GO-PA** | GO-crosslinked DNA polyaptamer |
| **GO-SC** | GO-crosslinked scrambled hydrogel |
| **HA** | hyaluronic acid |
| **HMA** | HA-coated, Mu-condensed, dual ASO-hybridized DNA |
| **Kan** | kanamycin |

| | |
|---|---|
| **MA** | Mu-condensed, dual ASO-hybridized DNA |
| **PCNA** | proliferating cell nuclear antigen |
| **PE** | phycoerythrin |
| **PNTrGO** | polyaptamer-anchored reduced graphene oxide |
| **PCNA** | proliferating cell nuclear antigen |
| **PNTrGO** | polyaptamer-anchored reduced graphene oxide |
| **PTK7** | protein tyrosine kinase 7 |
| **RCA** | rolling circle amplification |
| **rGO** | reduced graphene oxide |
| **ROX** | 6-carboxy-x-rhodamine |
| *S. aureus* | *Staphyloccocus aureus* |
| **SEM** | scanning electron microscopy |
| **SNTrGO** | scrambled polyaptamer-anchored reduced graphene oxide |
| **ssDNA** | single-stranded DNA |
| **TEM** | transmission electron microscopy |
| **TUNEL** | terminal deoxynucleotidyl transferase dUTP nick-end labeling |
| **XRD** | X-ray diffraction |

# Chapter I

# Overview

# 1. Introduction

Rolling circle amplification (RCA) is an isothermal, enzymatic process mediated by unique DNA and RNA polymerases ($\pi$29, Bst, and Vent exo-DNA polymerase for DNA, and T7 RNA polymerase for RNA) to generate long single stranded DNA (ssDNA) and RNA [1]. In a typical RCA reaction, the polymerase continuously adds nucleotides (nt) to the primer annealed to a circular template, resulting in replicating the circular template hundreds to thousands of times (Fig. I-1). Therefore, the end products of an RCA reaction are extremely long ssDNA molecules (usually hundreds of thousands of nucleotides and between hundreds of nanometers and microns in length) with tandem repeat units that are complementary to the circular DNA template.

As a method for molecular amplification, RCA has several attractive features. Unlike the polymerase chain reaction, which requires a thermal cycler and thermostable DNA polymerase, RCA utilizes the isothermal nature of $\pi$29 DNA polymerase, which catalyzes DNA polymerization at a constant temperature (at 30°C or even room temperature) [2]. Therefore, neither thermally stable DNA polymerase nor sophisticated instrumentation is required. In addition, RCA-based assays offer both high sensitivity and high specificity. As a method for signal amplification through either linear amplification or exponential growth, RCA typically provides an approximately 1,000-fold (for linear amplification) to 10,000-fold increase in the intensity of the signal [3]. Since RCA reaction can only be initiated after specific hybridization between a primer and the circular DNA template,
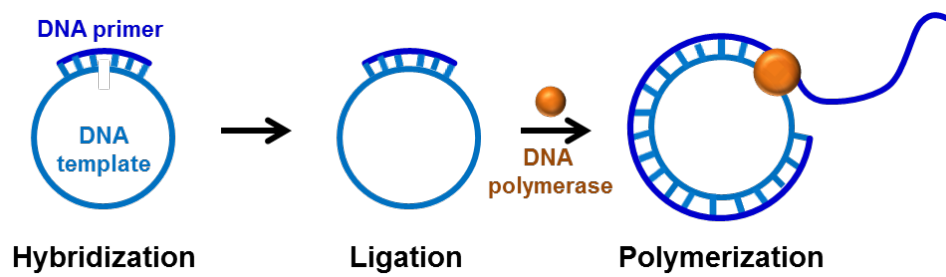
**Fig. I-1. Scheme of RCA by π29 DNA polymerase**

an RCA-based assay is highly specific [4]. Furthermore, by designing the circular DNA templates and primers, the length, sequence, composition, structure, and rigidity of the RCA product can be finely tuned [5]. Collectively, efficient isothermal amplification, single molecule sensitivity/selectivity, structural and compositional versatility, and multivalency make RCA a powerful tool in biomedical and nanotechnology fields.

RCA has traditionally been used for ultrasensitive detection methods of DNA [6], RNA [7], DNA methylation [8], small molecules [9], proteins [10], and cells [11] in areas of diagnostic genomics and proteomics. More recently, RCA has also attracted significant attention for its use in generating DNA nanostructures such as origami [12], nanotubes [13], DNA nanoscaffolds [14] for periodic nanoassembly, and DNA large-scale (micro- or macroscale) materials [15]. Furthermore, RCA has been used for amplifying functional sequences including DNA aptamers [16], DNAzymes [17], and restriction enzyme sites [18]. These functional RCA-based nanotechnologies have been utilized for biorecognition, imaging, and biosensor as well as drug delivery.

# 2. Biomedical applications of RCA-based nanotechnologies

RCA has currently been used for biomedical applications such as target cancer cell recognition, bioimaing, and biosensor, as listed in Table I-1.

## 2.1. Target cancer cell recognition

The development of a method for accurate, sensitive, selective, and rapid recognition and quantitation of cancer cells is important for the early diagnosis, treatment, and mechanistic studies [19]. Currently, there are conventional technologies for capture and isolation of cancer cells including the polymerase chain reaction, immunohistochemistry, and flow cytometry [20]. However, some of those methods require relatively complicated, time-consuming and inefficient methods, while others still have unsatisfactory sensitivity and specificity. To overcome these problems, RCA method have recently been investigated and developed to enhance the efficiency of signal amplification [21].

Sheng et al. developed a platform approach to recognize target cancer cells using RCA-directed enzyme-catalyzed polymerization [22]. To detect human breast cancer MCF-7 cells, a hairpin-structured aptamer with a strong binding affinity and selectivity to protein receptor was used. In the presence of the target cancer cell, RCA reaction can trigger enzymatically catalyzed polymerization by releasing cancer cells form electrode surface. For sensitive and selective recognition of Ramos cancer cells, bio-bar-code nanoprobe-based RCA nanotechnology was utilized. The dual-aptamer was used for improving selective

**Table I-1. RCA-based nucleic acid nanotechnologies for biomedical applications**

| Application | Conjugation | Functional domain | Reference |
|---|---|---|---|
| **Target cancer cell recognition** | Thiol-C6 | SYL3C aptamer | [22] |
| | AuNP | TD05, TE02 aptamer | [23] |
| | Polystyrene microspheres | TD05 aptamer | [24] |
| | Biotin | Sgc8 aptamer | [25] |
| **Bioimaging** | Protein matrix | miR-222 | [32] |
| | Antibody | Fluorescence probe | [33] |
| | - | *Mycobacterium tuberculosis* DNA | [34] |
| | - | Neuraminidase viral RNA | [35] |
| | - | Target mRNA | [36] |
| **Biosensor** | - | Pyrophosphate | [38] |
| | Antibody | SYBR/DNA conjugate | [39] |
| | - | Deoxyribozyme | [40] |
| | Biotin | 16S rDNA | [41] |

recognition of cancer cells. Amplified signals were measured by observing the chemiluminescence intensity change [23]. The RCA technique was combined with oligonucleotide functionalized nanoparticles, and the signal amplification systems exhibited high sensitivity and specificity with the detection limits of 10 Ramos cells ml$^{-1}$ [24]. Zhao et al. developed multivalent DNA network for recognition and release of cancer cells. The DNA network was synthesized by RCA, and comprised of repeating adhesive aptamer domain [25].

## 2.2. Bioimaging

The ability of visualizing targeted biomolecules at the single-cell level is essential for understanding the biological roles of biomolecules and diagnosing diseases [26]. To achieve ultrasensitive visualization of biomolecules, the probes to selectively bind and label the biomolecules were widely used. Although probes conjugated with nanostructure reporters such as metallic nanoparticles [27], quantum dots [28], nanocrystals [29], and nanodiamonds [30] have been developed to improve signal-to-noise ratio, these solid-core labels tend to aggregate and form nonspecific bindings with surfaces and other molecules [31]. To overcome the challenging barriers for single molecule probes, RCA has been well studied and used in bioimaging.

A study reported that target-primed RCA method can visualize miRNA expression patterns at the single-cell level with high sensitivity and selectivity [32]. After hybridization with fluorescent detection probes, target miRNA molecules can be visualized with ultrahigh sensitivity. For investigation of systematic cell

7

signaling, a proximity ligation technique was combined with RCA [33]. In cases where two differently labeled secondary antibodies are in close proximity, the oligonucleotide sequences can be amplified by means of RCA. This product is easily detected through hybridization of complementary fluorescence-labeled oligonucleotides. Chen's group developed polymeric sequence probe which was prepared by RCA [34, 35]. Since polymeric sequence probe has ~2000 tandem repeat target-binding sequences and label-binding sequences, it provided higher specific binding rates and strong fluorescence signal and single molecules such as DNA of *Mycobacterium tuberculosis* and viral RNA of influenza A can be clearly detected. In addition, Larsson et al. demonstrated that RCA technique was used for visualization of individual mRNA molecules [36].

## 2.3. Biosensor

RCA can amplify a single molecular binding event over a thousand fold, making it ideal for biosensing assay. The isothermal nature of RCA provides new possibilities for point-of-care diagnostics compared to other techniques such as PCR and enzyme-linked immunosorbent assay that use sophisticated and expensive instruments [37]. Due to these attractive features, RCA has been a promising analytical method for the detections of nucleic acids as well as other biomolecules, including protein, RNA, pathogen, and small molecules.

Mashimo et al. demonstrated that a bioluminescence assay combined with RCA can be used for quantitative analysis of miRNA [38]. The sensor was capable of detecting specifically as low as 0.1 fmol of a target small RNA within a total RNA

extract with high reproducibility. Cascade fluorescent DNA nanotags can be utilized for sensitive protein detection using streptavidin conjugated antibodies that carry multiple RCA primers [39]. For detection of small molecule such as guanosine triphosphate, Li and co-workers have applied a strategy to convert a kinase DNAzyme into RCA-based sensor [40]. A surface plasmon resonance DNA biosensor based on RCA with a gold nanoparticle surface was developed for isothermal identification of pathogenic microorganisms [41].

# 3. RCA-based nucleic acid nanostructures for drug delivery

RCA has been used for amplifying functional sequences including DNA aptamers, DNAzymes, and restriction enzyme sites. These functional RCA-based nanotechnologies have been utilized for drug delivery, as listed in Table I-2.

## 3.1. Nucleic acid drug delivery

Assembly of DNA nanoribbon structures with RCA have recently been developed for delivery of CpG oligonucleotide (ODN) [42, 43]. To prepare various types of DNA nanoribbon structures with RCA product, the researchers used various short staple oligonucleotides. In this study, they demonstrated that their 16 nm DNA origami nanoribbons showed more efficient cellular uptake and improved the release of TNF-α from RAW264.7 cells than single ss- or dsDNA, suggesting that these nanoribbons are resistant to nuclease degradation.

Long ssRNA produced by RCA using T7 RNA polymerase instead of π29 DNA polymerase had been designed for RNA-DNA hybrid nanowires [44]. Various types of RNA-DNA hybrid origami nanostructures were prepared using different kinds of staple short DNAs. The RNA-DNA hybrid nanowires have potential in delivery of small interfering RNA (siRNA).

Y-shaped DNA nanostructures self-assembled were prepared by RCA following to site-specific restriction cleavage [45]. The Y-shaped DNA nanostructures had a three-way junction in a core and three hairpin loops in arms which hybridized with folic acid conjugated siRNA containing its complementary overhangs. These Y-shaped DNA nanostructures hybridized with folic acid conjugated siRNA against

**Table I-2. Drug delivery systems based on RCA nanotechnology**

| Drug | Nanostructure | Composition | Reference |
|------|---------------|-------------|-----------|
| CpG ODN | Nanoribbon | Staple DNA strand | [42, 43] |
| siRNA | Nanowire | RNA-DNA hybrid | [44] |
| siRNA | Y-shaped DNA | Folic acid | [45] |
| siRNA | RNA microsponge | PEI | [46] |
| ASO | DNA microsponge | PEI, PLL | [47] |
| Dox | Linear poly-aptamer | Drug loading strand | [48] |
| Dox | DNA nanoflower | Multicolor molecules | [49, 50] |
| Dox | DNA nanoclew | DNase I, folic acid | [51] |
| Dox | DNA origami | AuNP, CPP, staple DNA strand | [52] |

GFP showed higher gene silencing effect compared to folic acid modified siRNA alone when they were treated to GFP-KB cells.

Hammond's group developed self-assembled RNA microsponges for siRNA delivery [46]. The RNA microsponges were synthesized by RNA technique and contained antisense and sense sequences of siRNA. These RNA microsponges were condensed by mixing with a synthetic cationic polymer, polyethylenimine (PEI), for increase of transfection efficiency. Moreover, antisense oligonucleotides were also delivered via the spherical microsponges [47]. Here, the RCA products were long ssDNA which contained antisense ODN. The antisense ODN microsponges were condensed via complexation with poly-L-lysine (PLL) which is synthetic cationic polymer. The ODN particles were coated with short ssDNA through electrostatic interactions. Finally, PEI was added to the ODN/PLL/ssDNA particles to generate layer-by-layer ODN nanoparticles for efficient delivery of antisense ODN.

## 3.2. Small molecule drug delivery

The RCA products have been used not only for nucleic acid drug delivery, but also for chemical drug delivery. A polyvalent aptamer system delivered an anticancer drug, doxorubicin (Dox), in a targeted delivery manner [48]. They used the property of Dox which can be intercalated to ssDNA for loading the drug to RCA product. The spacer region between one aptamer and another aptamer was hybridized its complementary strand for Dox loading. The polyvalent aptamer delivered the anticancer agent to protein tyrosine kinase 7 (PTK7), which binds to the aptamer, overexpressing cells. Similar approaches with DNA nanostructures

called "DNA nanoflowers" were developed for targeted drug delivery [49, 50]. They designed the template sequences for RCA including anti-PTK7 aptamer and drug loading sites. These DNA nanoflowers were used both for Dox delivery and cellular imaging by using fluorescent dye conjugated dUTP during RCA reaction.

The self-degradable DNA nanostructures in low pH environment were prepared by combining RCA products capable to load anticancer drug, Dox, and acid-responsive polymeric nanocapsules including DNase I [51]. DNase I was incorporated into the positively charged thin polymeric shells that was cross-linked by acid-degradable cross-linkers. To achieve active tumor targeting delivery of anticancer drug, folic acid was conjugated with DNA oligomer which was complementary to the DNA nanoclews. The study demonstrated that Dox could be released from their DNA nanoclews which had been taken up by MCF-7 cells via receptor mediated endocytosis because the DNase I was activated due to the low pH of endosomes.

The DNA origami structures produced by RCA with three staple strands also have been used to decorate on gold nanoparticles [52]. The DNA origami, which was about 16 nm in width and several hundred nanometers in length, let the nanoparticles be able to carry Dox for anticancer therapy or quantum dot for cellular imaging. Cell-penetrating peptides (CPP) were introduced to the DNA origami structures via electrostatic interactions to enhance the cellular uptake of the nanoparticles. A few drug delivery systems have been produced by RCA so far, however, these approaches are still at an early stage to develop drug delivery systems.

# 4. Scope of the studies

For biomedical applications, DNA nanomaterials have attracted tremendous interest, owing to the typical biocompatibility and biodegradability. In particular, the DNA amplification technique, RCA, can produce a long single stranded DNA using a circular DNA template and special DNA polymerase. Since RCA products can be tailor-designed by manipulating the circular template, RCA has been employed to generate complex DNA nanostructures and functional sequences. All these properties make multifunctional DNA nanostructures promising for versatile biomedical applications. As a proof-of-principle demonstration, in this study, DNA nanostructures were integrated with antisense oligonucleotides (ASOs), DNA aptamers, and drug loading sites, and the resultant functional DNA nanostructures were used to explore new approaches for drug delivery (Fig. I-2).

In chapter II, we designed biomimetic DNA nanoballs for delivery of multiple ASOs. Hyaluronic acid (HA)-coated, Mu peptide-condensed, dual ASO-loaded DNA nanoballs (HMA nanoballs) showed considerable cellular entry of Cy5-incorporated RCA product DNA and fluorescent ASOs. Dual ASOs, Dz13 and OGX-427, delivered by HMA nanoballs could reduce the levels of protein targets and exert anticancer effects.

In chapter III, we reported reduced graphene oxide nanosheets anchoring receptor-specific polyaptamer nanothreads (PNTrGO) for targeted drug delivery. PTK7 polyaptamer nanothreads with 22-mer oligoT bridges showed higher anchoring capacity onto rGO nanosheets. In CCRF-CEM leukemia cells
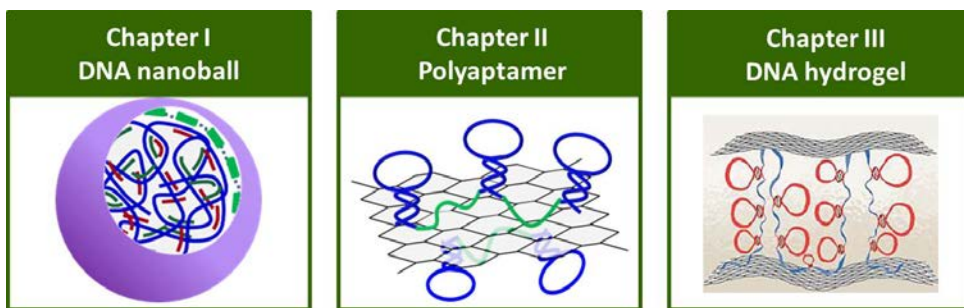
**Fig. I-2. Application of RCA-based DNA nanostructures**

overexpressing PTK7, the uptake of PNTrGO was 2.1-fold higher than that of oligoT-bridged scrambled polyaptamer-anchored rGO after 15 min pulse.

In chapter IV, we developed an injectable hydrogel based on drug-specific DNA polyaptamer networks using graphene oxide nanosheets as a crosslinker. Graphene oxide-crosslinked DNA polyaptamer (GO-PA) hybrid hydrogels revealed bird nest-like surface morphology, 700 % of swelling ratios in 2 hr, and viscoelasticity suitable for injection and retention. GO-PA hybrid hydrogel showed drug-specificity towards kanamycin and the drug loading efficiency of GO-PA was 58.0 % for kanamycin.

# 5. References

[1]    Liu M, Song J, Shuang S, Dong C, Brennan JD, Li Y. A graphene-based biosensing platform based on the release of DNA probes and rolling circle amplification. ACS Nano. 2014; 8(6):5564-5573.

[2]    Deng R, Tang L, Tian Q, Wang Y, Lin L, Li J. Toehold-initiated rolling circle amplification for visualizing individual microRNAs in situ in single cells. Angew Chem Int Ed Engl. 2014; 53(9):2389-2393.

[3]    Jin G, Wang C, Yang L, Li X, Guo L, Qiu B, Lin Z, Chen G. Hyperbranched rolling circle amplification based electrochemiluminescence aptasensor for ultrasensitive detection of thrombin. Biosens Bioelectron. 2015; 63:166-171.

[4]    Zhang LR, Zhu G, Zhang CY. Homogeneous and label-free detection of microRNAs using bifunctional strand displacement amplification-mediated hyperbranched rolling circle amplification. Anal Chem. 2014; 86(13):6703-6709.

[5]    Zhu G, Hu R, Zhao Z, Chen Z, Zhang X, Tan W. Noncanonical self-assembly of multifunctional DNA nanoflowers for biomedical applications. J Am Chem Soc. 2013; 135(44):16438-16445.

[6]    Russell C, Welch K, Jarvius J, Cai Y, Brucas R, Nikolajeff F, Svedlindh P, Nilsson M. Gold nanowire based electrical DNA detection using rolling

circle amplification. ACS Nano. 2014; 8(2):1147-1153.

[7]     Hong CY, Chen X, Li J, Chen JH, Chen G, Yang HH. Direct detection of circulating microRNAs in serum of cancer patients by coupling protein-facilitated specific enrichment and rolling circle amplification. Chem Commun (Camb). 2014; 50(25):3292-3295.

[8]     Geng Y, Wu J, Shao L, Yan F, Ju H. Sensitive colorimetric biosensing for methylation analysis of p16/CDKN2 promoter with hyperbranched rolling circle amplification. Biosens Bioelectron. 2014; 61:593-597.

[9]     Y, Li L, Yi X, Guo L. Label-free picomolar detection of Pb2+ using atypical icosahedra gold nanoparticles and rolling circle amplification. Biosens Bioelectron. 2014; 59:314-320.

[10]    Zhang X, Chen J, Liu H, Zhang S. Quartz crystal microbalance detection of protein amplified by nicked circling, rolling circle amplification and biocatalytic precipitation. Biosens Bioelectron. 2014; 65C:341-345.

[11]    Sheng Q, Cheng N, Bai W, Zheng J. Ultrasensitive electrochemical detection of breast cancer cells based on DNA-rolling-circle-amplification-directed enzyme-catalyzed polymerization. Chem Commun (Camb). 2015; 51(11):2114-2117.

[12]    Ma Y, Zheng H, Wang C, Yan Q, Chao J, Fan C, Xiao SJ. RCA strands as scaffolds to create nanoscale shapes by a few staple strands. J Am Chem Soc.

2013; 135(8):2959-2962.

[13] Hamblin GD, Hariri AA, Carneiro KM, Lau KL, Cosa G, Sleiman HF. Simple design for DNA nanotubes from a minimal set of unmodified strands: rapid, room-temperature assembly and readily tunable structure. ACS Nano. 2013; 7(4):3022-3028.

[14] Wang F, Willner B, Willner I. DNA nanotechnology with one-dimensional self-assembled nanostructures. Curr Opin Biotechnol. 2013; 24(4):562-574.

[15] Qi H, Ghodousi M, Du Y, Grun C, Bae H, Yin P, Khademhosseini A. DNA-directed self-assembly of shape-controlled hydrogels. Nat Commun. 2013; 4:2275.

[16] Lv L, Guo L, Zhao Q. Aptamer and rolling circle amplification-involved sandwich assay for platelet-derived growth factor-BB with absorbance analysis. Anal Methods. 2015; 7:1855-1859.

[17] Wang F, Lu CH, Liu X, Freage L, Willner I. Amplified and multiplexed detection of DNA using the dendritic rolling circle amplified synthesis of DNAzyme reporter units. Anal Chem. 2014; 86(3):1614-1621.

[18] Zhao W, Gao Y, Kandadai SA, Brook MA, Li Y. DNA polymerization on gold nanoparticles through rolling circle amplification: towards novel scaffolds for three-dimensional periodic nanoassemblies. Angew Chem Int Ed Engl. 2006; 45(15):2409-2413.

[19] Plaks V, Koopman CD, Werb Z. Cancer. Circulating tumor cells. Science. 2013; 341(6151):1186-1188.

[20] Wang J, Qu X. Recent progress in nanosensors for sensitive detection of biomolecules. Nanoscale. 2013; 5(9):3589-3600.

[21] Zhou G, Lin M, Song P, Chen X, Chao J, Wang L, Huang Q, Huang W, Fan C, Zuo X. Multivalent capture and detection of cancer cells with DNA nanostructured biosensors and multibranched hybridization chain reaction amplification. Anal Chem. 2014; 86(15):7843-7848.

[22] Sheng Q, Cheng N, Bai W, Zheng J. Ultrasensitive electrochemical detection of breast cancer cells based on DNA-rolling-circle-amplification-directed enzyme-catalyzed polymerization. Chem Commun (Camb). 2015; 51(11):2114-2117.

[23] Bi S, Ji B, Zhang Z, Zhang S. A chemiluminescence imaging array for the detection of cancer cells by dual-aptamer recognition and bio-bar-code nanoprobe-based rolling circle amplification. Chem Commun (Camb). 2013; 49(33):3452-3454.

[24] Ding C, Liu H, Wang N, Wang Z. Cascade signal amplification strategy for the detection of cancer cells by rolling circle amplification and nanoparticles tagging. Chem Commun (Camb). 2012; 48(41):5019-5021.

[25] Zhao W, Cui CH, Bose S, Guo D, Shen C, Wong WP, Halvorsen K,

Farokhzad OC, Teo GS, Phillips JA, Dorfman DM, Karnik R, Karp JM. Bioinspired multivalent DNA network for capture and release of cells. Proc Natl Acad Sci U S A. 2012; 109(48):19626-19631.

[26] Raj A, van den Bogaard P, Rifkin SA, van Oudenaarden A, Tyagi S. Imaging individual mRNA molecules using multiple singly labeled probes. Nat Methods. 2008: 5(10):877-879.

[27] Thompson DG, Enright A, Faulds K, Smith WE, Graham D. Ultrasensitive DNA detection using oligonucleotide-silver nanoparticle conjugates. Anal Chem. 2008; 80(8):2805-2810.

[28] Wang L, Liu S1, Liang W1, Li D1, Yang J2, He Y3. Detection of DNA utilizing a fluorescent reversible change of a biosensor based on the electron transfer from quantum dots to polymyxin B sulfate. J Colloid Interface Sci. 2015; 448:257-264.

[29] Ju Q, Uddayasankar U, Krull U. Paper-based DNA detection using lanthanide-doped LiYF4 upconversion nanocrystals as bioprobe. Small. 2014; 10(19):3912-3917.

[30] Gaillard C, Girard HA, Falck C, Paget V, Simic V, Ugolin N, Bergonzo P, Chevillard S, Arnault JC. Peptide nucleic acid–nanodiamonds: covalent and stable conjugates for DNA targeting. RSC Adv. 2014; 4:3566.

[31] Takimoto T, Chano T, Shimizu S, Okabe H, Ito M, Morita M, Kimura T,

Inubushi T, Komatsu N. Preparation of fluorescent diamond nanoparticles stably dispersed under a physiological environment through multistep organic transformations. Chem Mater. 2010; 22:3462-3471.

[32]  Ge J, Zhang LL, Liu SJ, Yu RQ, Chu X. A highly sensitive target-primed rolling circle amplification (TPRCA) method for fluorescent in situ hybridization detection of microRNA in tumor cells. Anal Chem. 2014; 86(3):1808-1815.

[33]  Blazek M, Betz C, Hall MN, Reth M, Zengerle R, Meier M. Proximity ligation assay for high-content profiling of cell signaling pathways on a microfluidic chip. Mol Cell Proteomics. 2013; 12(12):3898-3907.

[34]  Huang S, Yu C, Cheng G, Chen Y. Detection of single influenza viral RNA in cells using a polymeric sequence probe. Anal Chem. 2012; 84(19):8118-8121.

[35]  Huang S, Chen Y. Polymeric sequence probe for single DNA detection. Anal Chem. 2011; 83(19):7250-7254.

[36]  Larsson C, Grundberg I, Söderberg O, Nilsson M. In situ detection and genotyping of individual mRNA molecules. Nat Methods. 2010; 7(5): 395-397.

[37]  Kobori T, Takahashi H. Expanding possibilities of rolling circle amplification as a biosensing platform. Anal Sci. 2014; 30(1):59-64.

[38] Mashimo Y, Mie M, Suzuki S, Kobatake E. Detection of small RNA molecules by a combination of branched rolling circle amplification and bioluminescent pyrophosphate assay. Anal Bioanal Chem. 2011; 401(1): 221-227.

[39] Xue Q, Wang Z, Wang L, Jiang W. Sensitive detection of proteins using assembled cascade fluorescent DNA nanotags based on rolling circle amplification. Bioconjug Chem. 2012; 23(4):734-739.

[40] McManus SA, Li Y. Turning a kinase deoxyribozyme into a sensor. J Am Chem Soc. 2013; 135(19):7181-7189.

[41] Shi D, Huang J, Chuai Z, Chen D, Zhu X, Wang H, Peng J, Wu H, Huang Q, Fu W. Isothermal and rapid detection of pathogenic microorganisms using a nano-rolling circle amplification-surface plasmon resonance biosensor. Biosens Bioelectron. 2014; 62:280-287.

[42] Ouyang X, Li J, Liu H, Zhao B, Yan J, Ma Y, Xiao S, Song S, Huang Q, Chao J, Fan C. Rolling circle amplification-based DNA origami nanostructrures for intracellular delivery of immunostimulatory drugs. Small. 2013; 9(18):3082-3087.

[43] Ouyang X, Li J, Liu H, Zhao B, Yan J, He D, Fan C, Chao J. Self-assembly of DNA-based drug delivery nanocarriers with rolling circle amplification. Methods. 2014; 67(2):198-204.

[44] Zheng HN, Ma YZ, Xiao SJ. Periodical assembly of repetitive RNA sequences synthesized by rolling circle transcription with short DNA staple strands to RNA-DNA hybrid nanowires. Chem Commun (Camb). 2014; 50(17):2100-2103.

[45] Hong CA, Jang B, Jeong EH, Jeong H, Lee H. Self-assembled DNA nanostructures prepared by rolling circle amplification for the delivery of siRNA conjugates. Chem Commun (Camb). 2014; 50(86):13049-13051.

[46] Lee JB, Hong J, Bonner DK, Poon Z, Hammond PT. Self-assembled RNA interference microsponges for efficient siRNA delivery. Nat Mater. 2012; 11(4):316-322.

[47] Roh YH, Lee JB, Shopsowitz KE, Dreaden EC, Morton SW, Poon Z, Hong J, Yamin I, Bonner DK, Hammond PT. Layer-by-layer assembled antisense DNA microsponge particles for efficient delivery of cancer therapeutics. ACS Nano. 2014; 8(10):9767-9780.

[48] Zhang Z, Ali MM, Eckert MA, Kang DK, Chen YY, Sender LS, Fruman DA, Zhao W. A polyvalent aptamer system for targeted drug delivery. Biomaterials. 2013; 34(37):9728-9735.

[49] Hu R, Zhang X, Zhao Z, Zhu G, Chen T, Fu T, Tan W. DNA nanoflowers for multiplexed cellular imaging and traceable targeted drug delivery. Angew Chem Int Ed Engl. 2014; 53(23):5821-5826.

[50]  Zhu G, Hu R, Zhao Z, Chen Z, Zhang X, Tan W. Noncanonical self-assembly of multifunctional DNA nanoflowers for biomedical applications. J Am Chem Soc. 2013; 135(44):16438-16445.

[51]  Sun W, Jiang T, Lu Y, Reiff M, Mo R, Gu Z. Cocoon-like self-degradable DNA nanoclew for anticancer drug delivery. J Am Chem Soc. 2014; 136(42):14722-14725.

[52]  Yan J, Hu C, Wang P, Zhao B, Ouyang X, Zhou J, Liu R, He D, Fan C, Song S. Growth and origami folding of DNA on nanoparticles for high-efficiency molecular transport in cellular imaging and drug delivery. Angew Chem Int Ed Engl. 2015; 54(8):2431-2435.

# Chapter II

# Biomimetic DNA nanoballs for oligonucleotide delivery

# 1. Introduction

Recently, functional oligonucleotides have been studied as a major class of nucleic acid-based therapeutics [1]. Antisense oligonucleotides (ASOs) and micro RNA are examples of oligonucleotides with therapeutic potentials. However, these oligonucleotides suffer from drawbacks, such as instability against nucleases and limited cellular uptake owing to their high negative charges. To overcome these drawbacks, researchers delivered oligonucleotides using cationic lipids or polymer-based delivery systems. Cationic nanoparticles have previously been used to deliver single stranded oligonucleotides based on charge-charge loading to cationic liposomes [2,3] and polymer-based nanoparticles [4,5]. However, the cationic nanoparticle-associated cytotoxicity [6] requires the development of other carriers not cationic as well as biomimetic for delivery of oligonucleotides.

Rolling circle amplification (RCA) is an enzymatic process that produces a single-stranded DNA (ssDNA) from a circular template. The resulting ssDNA is composed of complementary-sequence repeats of the circular template. RCA technology was originally used for DNA detection in genomics; however, additional applications using RCA have been reported [7]. Recently, RCA was applied to construct DNA nanostructures and DNA hydrogels [8-11].

In this study, we used RCA-amplified DNA to produce an oligonucleotide delivery system. As model oligonucleotides, we chose two ASO oligonucleotides. To load ASO to the delivery system, we used sequence-specific hybridization rather than cationic nanoparticle-based charge-charge interaction. The template for

RCA was designed to have complementary sequences for two different ASOs and to produce poly-binding sites for ASOs upon RCA amplification. Exploiting the DNA condensation mechanisms of viruses, we employed cationic Mu peptides derived from the adenovirus core complex to condense ASO-hybridized RCA products (ARP) and produce DNA nanoballs. The surface of ASO-loaded DNA nanoballs was coated with hyaluronic acid (HA), a ligand for CD44 receptors overexpressed by tumor cells [12], for tumor-targeted delivery.

Here, we demonstrated that DNA nanoballs with ASO-complementary sequences could provide sequence-specific loading of dual ASOs, and coating with HA promoted CD44 receptor-mediated delivery of ASOs to tumor cells. Importantly, ASOs delivered by HA-coated DNA nanoballs silenced the expression of their target mRNAs of ASO, exerting potent anticancer effects in vitro and in vivo.

# 2. Materials and methods

## 2.1. Construction of ASO-hybridized DNA nanoballs

ASO-hybridized DNA nanoballs were constructed by (1) amplifying ssDNA containing ASO-binding sites by RCA, (2) hybridizing with ASO, and (3) condensing with cationic Mu peptides. In the first step, an RCA template for complementary binding with ASOs was circularized using primers. Briefly, 0.5 μM of 5'-phosphorylated linear ssDNA template and primer (Macrogen Inc., Daejeon, Republic of Korea) were annealed in hybridization buffer (10 mM Tris-HCl, 1 mM EDTA, 100 mM NaCl, pH 8.0) and mixed with T4 DNA ligase (125 units/mL) (Thermo Scientific, Waltham, MA, USA) to close the nick in the circular RCA template. After inactivating T4 DNA ligase by heating to 70°C, the circular RCA template (200 μL) was incubated at 30°C for 12 h with π29 DNA polymerase (100 units/mL) (Thermo Scientific) and 2 mM dNTPs (Intron Biotechnology Inc., Seoul, Republic of Korea). In some experiments, fluorescent RCA products were prepared by adding 25 μM of Cy5-dCTP to 2 mM dNTPs during the RCA reaction. After heat-inactivating π29 DNA polymerase at 70°C for 10 min, residual dNTPs were removed by centrifugation at 13,000 rpm for 10 min. The resulting pellet of RCA product was resuspended in water, and its concentration was measured using a Nanodrop spectrophotometer (Thermo Scientific). Two different ASOs—Dz13 (125 μg) and OGX-427 (125 μg)—were hybridized with 1 mL of RCA products (500 μg DNA/mL) by heating at 95°C for 10 min and then cooling gradually at room temperature. The cationic Mu peptide (Peptron, Daejeon, Republic of Korea)

was added to the resulting dual ARP at a weight ratio of 1:1 to form a nanoball-like structure. The resulting complexes of Mu-condensed, dual ASO-hybridized DNA nanoballs (MA nanoballs) were mixed with 214 kDa HA (Lifecore Biomedical Inc., Chaska, MN, USA) at a DNA:Mu:HA weight ratio of 1:1:5. HA-coated, Mu-condensed, dual ASO-hybridized DNA nanoballs (HMA nanoballs) were stored at 4°C until use. In some experiments, RCA products alone were mixed with Mu peptide at a weight ratio of 1:1, and coated with HA at a DNA:Mu:HA ratio of 1:1:5 to produce HA-coated, Mu-condensed DNA nanoballs without ASOs (HM nanoballs).

## 2.2. Quantification of hybridized ASOs

The two ASOs, Dz13 and OGX-427, were labeled using different fluorescent dyes to measure the efficiency of hybridization to RCA products. Fluorescein (FAM)-conjugated Dz13 and 6-carboxy-x-rhodamine (ROX)-tagged OGX-427 were supplied by Bioneer Corporation (Daejeon, Republic of Korea). The fluorescent dye-modified ASOs, FAM-Dz13 and ROX-OGX-427 (5.5 µg each), were hybridized with 100 µL of RCA products (200 µg DNA/mL). The procedure described in section 2.1 was adopted for loading fluorescent dye-modified ASOs to RCA products. Unloaded fluorescent ASOs were removed by repeated centrifugation at 13,000 rpm for 10 min, and the fluorescence intensity of the supernatants was measured using a Spectramax Gemini XS microplate fluorometer (Molecular Devices Cooperation, Sunnyvale, CA, USA). The amounts of hybridized Dz13 and OGX-427 were calculated from calibration curves of

fluorescence intensity of each fluorescent dye-labeled ASO as a function of concentration.

## 2.3. Characterization study of DNA nanoballs

The sizes of various DNA nanoballs, with or without Mu peptide-induced condensation and HA coating, were measured by dynamic light scattering. The zeta potentials of DNA nanoballs were also measured by laser Doppler microelectrophoresis at an angle of 22° using an ELSZ-1000 instrument (Photal, Osaka, Japan). The morphology of DNA nanoballs was visualized by scanning electron microscopy (SEM) using a Supra 55VP system (Carl Zeiss, Oberkochen, Germany). The stability of ARP, MA nanoballs, and HMA nanoballs against nucleases was tested by incubating 1 μg of DNA with 1 unit of DNase I (Sigma, St. Louis, MO, USA) at 37°C for 30 min. The mixture was electrophoresed on 1% agarose gels and visualized by staining with Safe-Pinky dye (GenDepot, Barker, TX, USA).

## 2.4. Cellular uptake test of DNA nanoballs

Cellular uptake of various DNA nanoballs was evaluated by preparing fluorescent DNA nanoballs using 25 μM Cy5-dCTP (Perkin Elmer, Boston, MA, USA) and DNA nanoballs carrying fluorescent dye-modified ASOs, as described above. KB human epidermal carcinoma cells (American Type Culture Collection, Rockville, MD, USA) were cultured in RPMI-1640 medium (Welgene, Daegu, Korea) supplemented with 10 % fetal bovine serum and 100 units/mL penicillin

plus 100 μg/mL streptomycin. KB cells were seeded onto poly-L-lysine coated coverslips (BD Biosciences, San Jose, CA, USA) in 24-well plates (SPL Life Sciences, Pocheon, Republic of Korea) at a density of $8 \times 10^4$ cells/well. The next day, cells were treated with Cy5-dCTP–incorporated fluorescent DNA nanoballs or fluorescent dye-modified ASO-loaded DNA nanoballs at a concentration of 20 μg DNA/well. In some experiments, cells were pre-incubated with 10 μM HA for 2 h prior to treatment with DNA nanoballs. For fluorescence microscopy, cells were washed and fixed with 4 % paraformaldehyde in phosphate-buffered saline (PBS) for 15 min, and stained with 4',6-diamidino-2-phenylindole dihydrochloride (DAPI). The fluorescence of cells was observed using a confocal laser-scanning microscope (LSM 5 Exciter; Carl Zeiss, Inc., Jena, Germany). For flow cytometry, the cells were harvested and washed three times with cold PBS containing 2 % fetal bovine serum, and analyzed using a BD FACSCalibur system equipped with Cell Quest Pro software (BD Biosciences).

## 2.5. Knockdown study of target protein expression

In vitro silencing of target protein expression by DNA nanoballs was evaluated by Western blotting. Various DNA nanoballs were applied to KB cells seeded in 6-well plates. After 1 h incubation, the cell medium was replaced and cells were incubated for an additional 24 h. Whole-cell lysates were then prepared, and extracted proteins were quantified using a BCA protein assay kit (Thermo Scientific) according to the manufacturer's instruction. Proteins in samples were separated by sodium dodecyl sulfate-polyacrylamide gel electrophoresis

(SDS-PAGE) on 10 % gels and then transferred onto polyvinylidene difluoride membranes (Hybond-ECL; Amersham Biosciences, Piscataway, NJ, USA). Membranes were probed by Western blotting using specific antibodies to c-Jun (1:500, sc-1694; Santa Cruz Biotechnology, CA, USA), Hsp27 (1:500, sc-9012; Santa Cruz Biotechnology), and glyceraldehyde-3-phosphate dehydrogenase (GAPDH; 1:1000, sc25778; Santa Cruz Biotechnology).

## 2.6. Assessment of DNA nanoball anticancer activity

The cancer cell-killing effect of various DNA nanoballs was quantitatively evaluated using a Cell Counting Kit 8 (CCK-8; Dojindo Laboratories, Kumamoto, Japan) and visualized by staining of live cells after treatment with DNA nanoballs. KB cells were seeded in 48-well plates at a density of $6 \times 10^4$ cells/well. The next day, the cells were treated with various types of DNA nanoballs at a constant amount of DNA (20 μg/well). After a 1 h incubation in the presence or absence of 1 μM doxorubicin (Dox), the cell medium was replaced and cells were incubated for an additional 24 h. Cell viability was then measured by CCK-8 assay. For CCK-8 assays, 20 μL of CCK-8 solution was added to each well and plates were incubated for 30 min. The absorbance of the medium at 450 nm was then measured colorimetrically using an enzyme-linked immunosorbent assay (ELISA) reader (Sunrise-Basic TECAN, Mannedorf, Switzerland). For live cell staining, cells were stained with calcein-AM (Molecular Probes, Eugene, OR, USA) after treatment with various DNA nanoballs.

## 2.7. In vivo molecular imaging

The in vivo tumor distribution of Cy5-dCTP–labeled DNA nanoballs was assessed by molecular imaging. Five-week-old athymic nude mice (Orient Bio Inc., Seongnam, Korea) were subcutaneously inoculated with $5 \times 10^5$ KB cells. After tumors had reached a volume of ~100 mm$^3$, fluorescent HMA or MA nanoballs were intravenously injected into the mice at a dose of 4 mg DNA/kg. After 1 h, the intensity of Cy5 signals was monitored using an eXplore Optix system (Advanced Research Technologies Inc., Montreal, Canada) and scanned using a 670 nm laser at a power of 25 mW and a count time of 0.3 s/point.

## 2.8. In vivo study of anti-tumor effects

The in vivo anti-tumor activity of DNA nanoballs was evaluated by measuring tumor growth-inhibitory effects. KB cells ($5 \times 10^5$ cells) were subcutaneously inoculated into the dorsal right side of 5-wk-old athymic nude mice (Orient Bio). After tumors had become established, DNA nanoballs and Dox were intravenously administrated at a DNA dose of 8 mg/kg and a Dox dose of 3 mg/kg. For MA and HMA nanoballs, the doses of ASOs were 2 mg/kg each for Dz13 and OGX-427. Mice were treated with the mixture of DNA nanoballs and Dox every other day for a total of three injections. Tumor size was measured in two dimensions using a slide caliper every 2 days, and tumor volume was calculated as a × b × b × 0.5, where a and b are the lengths of the largest and smallest dimensions. The mice were sacrificed on day 14, and tumor tissues were extracted and weighed.

## 2.9. Statistics

All statistical analyses were performed using analysis of variance (ANOVA) with a post hoc Student–Newman–Keuls test. SigmaStat software (version 3.5; Systat Software, Richmond, CA, USA) was used for the analyses, and a p-value less than 0.05 was considered statistically significant.

# 3. Results

## 3.1. Sequence-specific hybridization of dual ASOs onto DNA nanoballs

The sequences of scrambled and dual ASO-complementary RCA templates are illustrated in Fig. II-1A and II-1B, respectively. ARP was formed by hybridization of Dz13 and OGX-427 (Fig. II-1C). Loading amounts of Dz13 and OGX-427 onto RCA products depended on the sequences of RCA templates. As compared to RCA products of scrambled template, the RCA products of dual ASO-complementary RCA templates provided 8.1- and 6.7-fold higher loading amounts for Dz13 and OGX-427, respectively (Fig. II-1D). ARP was then treated with adenovirus-derived Mu peptide to produce Mu peptide-condensed, dual ASO-loaded DNA nanoballs (MA nanoballs). HA was then complexed with MA nanoballs to form HA-coated, Mu peptide-condensed, dual ASO-loaded DNA nanoballs (HMA nanoballs) for targeted delivery of ASOs to tumors overexpressing the receptor, CD44.

## 3.2 Characterization of ASO-hybridized DNA nanoballs

The structures of various DNA nanoballs are illustrated in Fig. II-2A. Mu peptide-complexed ARP exhibited nanoball-like structures (Fig. II-2B, II-2C). Surface coating of MA nanoballs with HA retained nanoball-like structures (Fig. II-2B, II-2C). The size (Fig. II-2D) and zeta potential (Fig. II-2E) of ARP were 1,242.5 nm ± 320.4 nm and -29.1 mV ± 11.5 mV, respectively. Addition of cationic Mu peptide reduced the size to 162.7 nm ± 32.4 nm and increased the zeta potential to 5.0 mV ± 1.4 mV. After surface coating with HA, the size of nanoballs
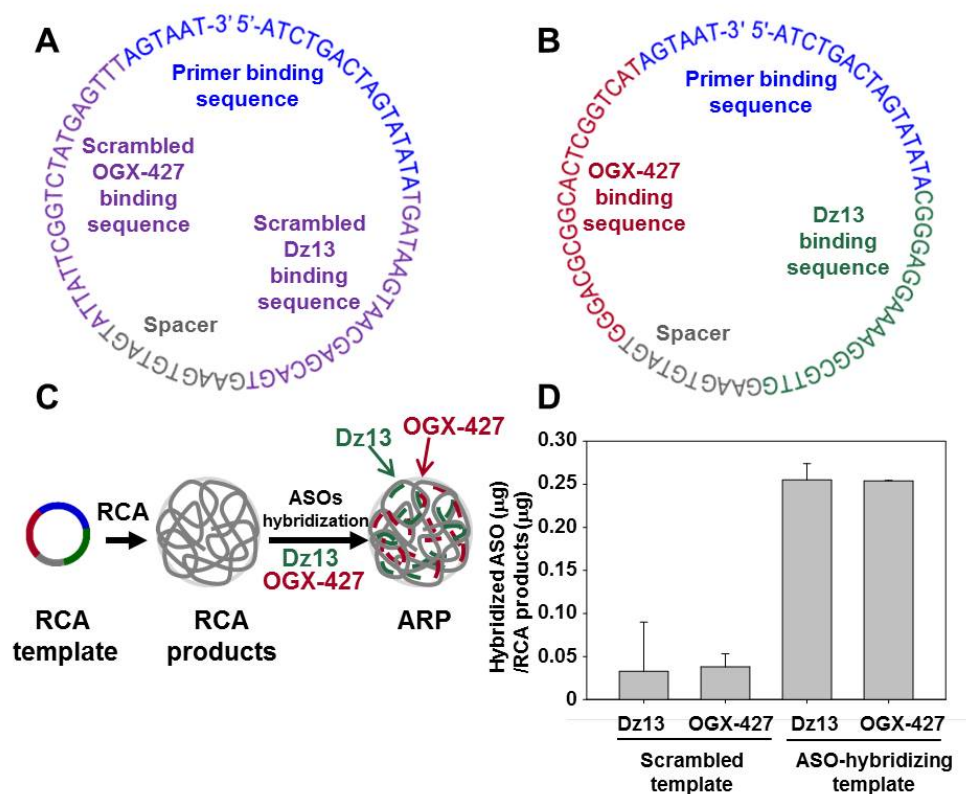
**Fig. II-1. RCA template and hybridization efficiency.**

(A) Secondary structure of scrambled RCA template. (B) Secondary structure of a dual ASO-hybridizing RCA template for Dz13 and OGX-427. (C) RCA products with poly ASO-binding sequences were hybridized with two ASOs, Dz13 and OGX-427, to produce dual ARP. (D) The hybridization efficiencies of the ASOs, Dz13 and OGX-427, were tested for products of scrambled RCA templates and dual ASO-hybridizing RCA templates using fluorescently labeled ASOs (FITC-Dz13, ROX-OGX-427).

was 191.4 nm ± 15.1 nm, and the zeta potential was -21.8 mV ± 0.7 mV. Both MA nanoballs and HMA nanoballs showed stability against nucleases (Fig. II-2F). Upon 30 min treatment with DNase I, ARP was completely degraded and migrated to the bottom of agarose gels. In contrast, agarose gel electrophoresis showed no degraded DNA fragments of MA nanoballs or HMA nanoballs after DNase I treatment. Thus, adenovirus-derived cationic Mu peptide substantially decreased the size of ARP, increased their zeta potential values, and provided stability against nuclease.

## 3.3. Cellular uptake of DNA nanoballs and dual ASOs

HMA nanoballs entered KB cells via CD44 receptors. To visualize and quantitate the cellular uptake of DNA nanoballs, we used Cy5-incorporated DNA nanoballs by running RCA using Cy5-dCTP. Confocal microscopy (Fig. II-3A) and flow cytometry (Fig. II-3B, II-3C) showed little uptake of Cy5-dCTP-incoroporated fluorescent ARP or MA nanoballs by CD44-overexpressing KB cells, but revealed considerable entry of fluorescent HMA nanoballs into KB cells. The enhanced cellular uptake of MA nanoballs caused by HA-coating was not observed when the cells were pretreated with free HA.

As a complementary approach, we examined cellular uptake of DNA nanoballs containing hybridized, fluorescently labeled ASOs. Consistent with the above results, confocal microscopy (Fig. II-4A) and flow cytometry showed considerable entry of FAM-conjugated Dz13 (Fig. II-4B) and ROX-conjugated OGX-427 (Fig.
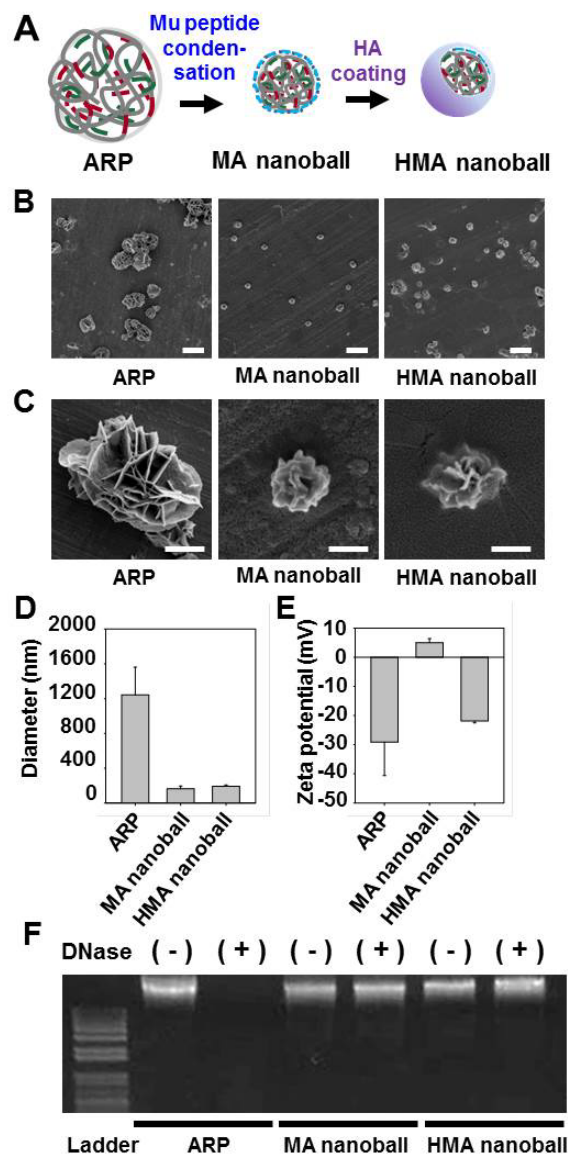
**Fig. II-2. Schematic illustration and morphology of DNA nanoballs.**

(A) Illustration of the HMA nanoball preparation scheme. Dual ARP were mixed

with adenovirus core complex-derived Mu peptide to form MA nanoballs. The

surfaces of MA nanoballs were coated with HA to produce HMA nanoballs. (B,C) The morphologies of ARP, MA nanoballs, and HMA nanoballs were observed by SEM at different magnifications. Scale bar: 2 um for all groups (B). Scale bar: 800 nm for ARP and 200 nm for MA nanoball and HMA nanoballs (C). (D) The sizes of ARP, MA nanoballs, and HMA nanoballs were measured by dynamic light scattering. (E) Zeta potential values of ARP, MA nanoballs, and HMA nanoballs were determined by laser Doppler microelectrophoresis. (F) The stability of ARP, MA nanoballs, and HMA nanoballs against DNase I was tested by incubation with 1 unit of DNase I for 30 min, followed by electrophoresis on a 1 % agarose gel.
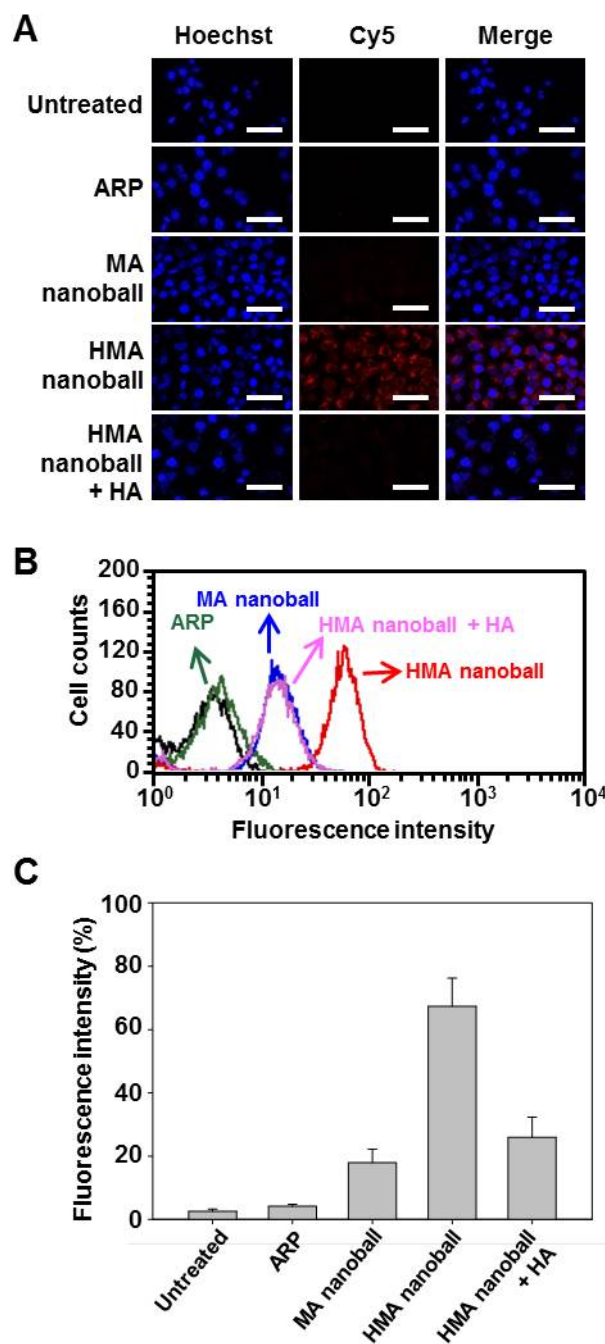
- continued next page -

**Fig. II-3. Cellular uptake of DNA nanoballs.**

KB cells were left untreated or were treated with ARP, MA nanoballs or HMA nanoballs, with or without HA pre-treatment. Cellular uptake of Cy5-incorporated fluorescent DNA nanoballs was visualized by confocal microscopy (A) and quantified by flow cytometry (B, C). (B) Representative flow cytometry data. (C) Quantification of populations of fluorescence-positive cells. Data are presented as means ± SE (n = 4). Scale bar: 20 μm.

II-4C) into CD44-overexpressing KB cells, but little uptake of these fluorescent ASOs when hybridized to MA nanoballs, which lack HA (Fig. II-4D). Again, this enhancement of cellular uptake of MA nanoballs by HA-coating was eliminated by pretreating cells with free HA. Collectively, these results confirm the CD44 receptor-dependence of HMA nanoball uptake.

## 3.4. Reduction of target protein expression by DNA nanoballs

We next investigated the effect of HMA nanoballs on the expression levels of proteins targeted by the dual hybridized ASOs: c-Jun, the target of the DNAzyme Dz13, and Hsp27, the target of OGX-427. Downregulation of target proteins was monitored by Western blotting (Fig. II-5), which showed that treatment of KB cells with HMA nanoballs decreased the protein levels of c-Jun and Hsp27 to 33.0 % ± 9.5 % (Fig. II-5A) and 12.6 % ± 7.2 % (Fig. II-5B) of control levels, respectively. In contrast, treatment of KB cells with HM or MA nanoballs alone did not significantly reduce the levels of either protein (Fig. II-5C).

## 3.5. In vitro anticancer effects of DNA nanoballs

Among the various DNA nanoballs, HMA nanoballs showed the greatest in vitro anticancer effect and synergized with Dox to further enhance anticancer efficacy. CCK-8 assay results reveal that the survival of KB cells was not significantly reduced by treatment with ARP, HM, or MA nanoballs (Fig. II-6A). However, treatment of KB cells with HMA nanoballs reduced the survival of KB cells to 69.3 % ± 1.7 % of control levels; co-treatment of KB cells with Dox and
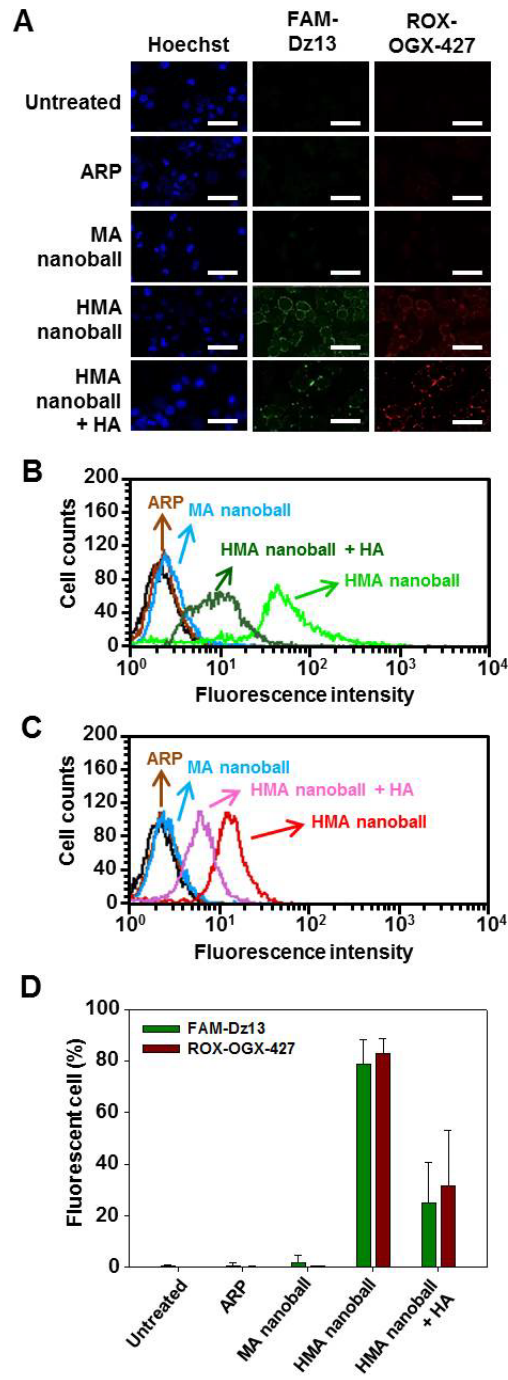
- continued next page -

**Fig. II-4. Cellular uptake of ASOs.**

KB cells were left untreated or were treated with ARP, MA nanoballs or HMA nanoballs, with or without HA pre-treatment. (A) Cellular uptake of FAM-Dz13 and ROX-OGX427 ASOs loaded in DNA nanoballs was visualized by confocal microscopy. (B, C) Representative flow cytometry data for cell populations positive for FAM-Dz13 (B) and ROX-OGX427 (C) under various conditions. (D) Flow cytometry-based quantification of populations of fluorescent (ASO-positive) cells. Data are presented as means ± SE (n = 3). Scale bar: 20 μm.
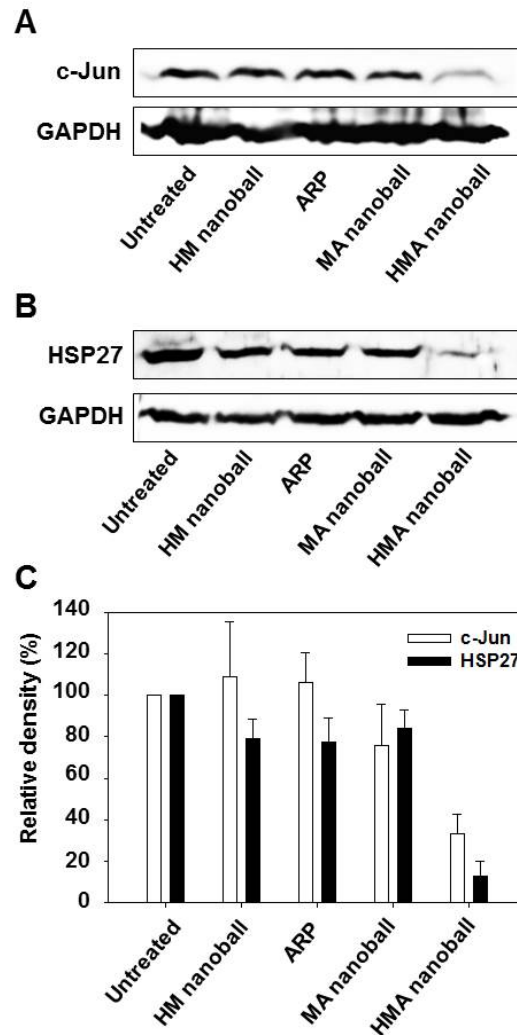
**Fig. II-5. Reduction of target proteins.**

The cellular protein levels of target genes, c-Jun (A) and Hsp27 (B), were measured by Western blotting. After various treatments, whole-cell extracts of KB cells were analyzed for target proteins by Western blotting. The data are expressed as means ± SE (n = 3). (C) Relative intensities of c-Jun and Hsp27 were normalized to the GAPDH signal.

HMA nanoballs further reduced survival to 51.5 % ± 5.1 % (Fig. II-6A). Similar to the CCK-8 assay results, the fluorescent microscopy of live cells exhibited the lowest live cell populations in the group treated with HMA nanoballs (Fig. II-6B).

## 3.6. Biodistribution and in vivo antitumor effects of DNA nanoballs

We next examined the effect of surface coating with HA on tumor tissue accumulation and antitumor effects of intravenously administered MA nanoballs. For molecular imaging, Cy5-incorporated fluorescent nanoballs were injected into KB cell tumor-bearing nude mice. The tumor tissue distribution of Cy5-incorporated HMA nanoballs 1 h post-dose was greater than that of Cy5-incorporated MA nanoballs (Fig. II-7A). At 24 h post-injection, total photon counts in tumor tissues were 5.9-fold higher in the HMA nanoball-treated group than in the MA nanoball-treated group (Fig. II-7B).

Collectively, these results indicate that surface coating of MA nanoballs with HA enhances tumor tissue accumulation. Systemic co-administration of HMA nanoballs with Dox synergistically inhibited tumor growth in a KB cell xenograft mouse model. Compared to other groups, the HMA nanoball-treated group showed the lowest tumor volume (Fig. II-8A) and weight (Fig. II-8B).
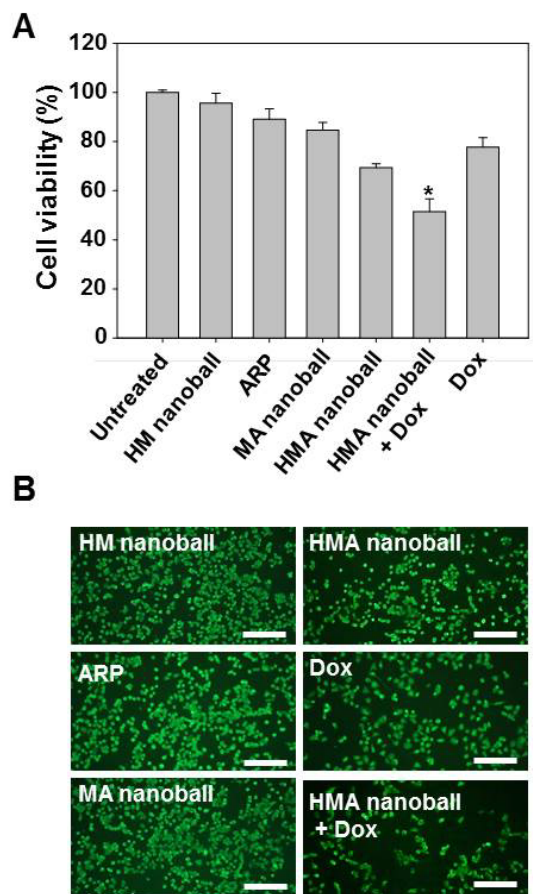
**Fig. II-6. In vitro tumor cell-killing effect.**

(A) KB cells were treated with ARP, MA nanoballs, HM nanoballs, or HMA nanoballs in the presence or absence of Dox for 1 h. After media replacement, the cells were incubated for an additional 24 h. The survival of cancer cells was determined by CCK-8 assay. Data are presented as means ± SE (n = 4). (B) The live cell population was stained with calcein-AM and observed by fluorescence microscopy. Scale bar: 20 μm.
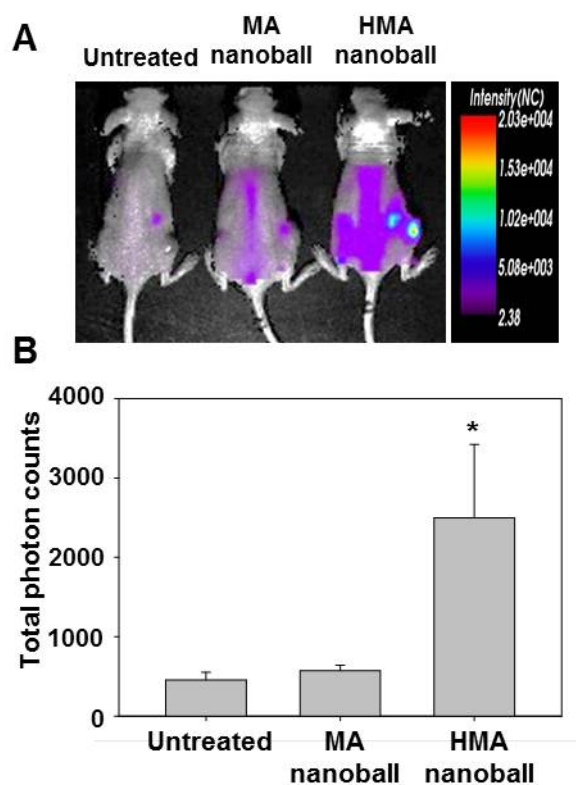
**Fig. II-7. Biodistribution of ASO-loaded DNA nanoballs.**

(A) KB tumor-bearing mice were intravenously injected with MA nanoballs or HMA nanoballs containing Cy5-dCTP. The biodistribution of Cy5 fluorescence was visualized using a molecular imaging system. (B) The total photon counts of tumor tissues from treated mice were quantified 1 h post-administration by in vivo imaging and compared with those of the untreated group.
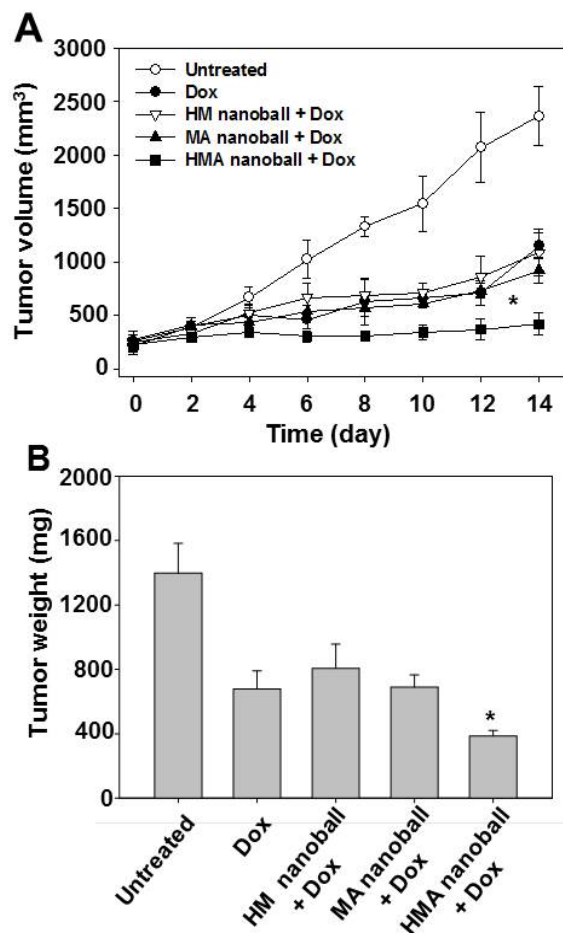
**Fig. II-8. In vivo antitumor effect of ASO-loaded DNA nanoballs.**

KB tumor-bearing mice were intravenously injected with HM nanoballs, MA nanoballs, or HMA nanoballs (8 mg DNA/kg) and Dox (3 mg Dox/kg) or with Dox alone (3 mg Dox/kg) every other day for a total of three injections. For MA and HMA nanoballs, the dose of both ASOs was 2 mg/kg. Tumor sizes were measured until day 14 (A), and tumor tissues were extracted and weighed (B).

# 4. Discussion

Here, we demonstrated that the adenovirus-derived Mu peptide played an essential role in condensing ARP to form MA nanoballs, and surface coating with HA promoted CD44 receptor-mediated delivery of HMA nanoballs to tumor cells. Importantly, ASOs delivered by HMA nanoballs silenced the expression of their target mRNAs of ASO, exerting potent anticancer effects in vitro and in vivo upon co-treatment with Dox.

The goal of this study was to test the delivery of therapeutic oligonucleotides via nucleic acid-based DNA nanoballs using sequence-specific hybridization as a loading technique. ssDNA amplified by a RCA reaction can serve as an ASO sequence-specific carrier owing to its thousands of complementary sequences to the ASO. Compared to a scrambled RCA template, RCA templates containing ASO-binding sequences hybridize substantially higher amounts of ASO per RCA product (Fig. II-1D). This high hybridization capacity supports the feasibility of using hybridization-mediated ASO loading of RCA products for sequence-specific ASO delivery.

Dual ASOs—Dz13 and OGX-427—were loaded onto HMA nanoballs in a sequence-specific manner (Fig. II-1B). Dz13 is a DNAzyme with RNA-binding hybridization arms that cleaves the mRNA of c-Jun, which is involved in cellular proliferation, transformation, and cell death [13]. OGX-427 is known to inhibit the expression of Hsp27, which is involved in cancer progression and cell death [14].

The adenovirus core complex-derived Mu peptide was used for biomimetic condensation of micrometer- to nanometer-sized DNA balls (Fig. II-2). In the

absence of Mu peptide, the dual ASO-loaded ssDNAs tended to form a soft, "ball" in solution with a diameter of approximately 1.5 μm (Fig. II-2C). Our observations are consistent with a previous report, which showed that micrometer-sized DNA balls are produced by a RCA reaction [15, 16].The interaction between ARP and cationic Mu peptides is electrostatic, resulting in an increase in the zeta potential after condensation (Fig. II-2D).

We observed that uptake of ASO by CD44 receptor-overexpressing KB cells was enhanced by delivery using HMA nanoballs compared with MA nanoballs (Fig. II-3 and II-4), supporting the role of the HA moiety in enhancing CD44 receptor-mediated cellular delivery of DNA nanoballs. HA has been previously reported to increase the tumor cell delivery of nanoparticles by interacting with CD44 receptors; when conjugated to ASOs, it enhances their cellular delivery [17].

The reduction in target protein levels after treatment of cells with HMA nanoballs is attributable to the enhanced uptake of nanoballs via the HA moiety and implies effective delivery of ASOs to the interior of the cell. The reduced cellular uptake of HMA nanoballs (Fig. II-3) and ASO (Fig. II-4) after pretreatment with HA supports the conclusion that the entry of HMA nanoballs into KB cells is mediated by the CD44 receptor. Although further study will be required to elucidate the intracellular fate of HMA nanoballs, we speculate that HMA nanoballs may be partially degraded in endolysosomes, enabling escape of ASOs into the cytosol and binding to target mRNA.

Owing to the greater affinity of the ASOs, Dz13 and OGX-427, for their target mRNA compared to that for the complementary ASO-binding sequence, the uptake

of HMA nanoballs into cells resulted in the dissociation of ASOs from HMA nanoballs and binding to their target mRNA. In addition to the natural preference of ASOs for their natural target mRNAs, dissociation of ASOs from ARP was further facilitated by modifying the RCA template for complementary binding with ASO to contain one mismatched base pair for each ASO. Such facilitated dissociation caused by a single mismatch has been previously demonstrated [18].

We observed the greatest in vivo antitumor effect following combined treatment with Dox and HMA nanoballs (Fig. II-8). The target proteins of two ASOs, Dz13 and OGX-427, have been reported to be involved in the anticancer mechanisms by Dox [26, 27]. Treatment of small lung cancer cells with Dox was shown to induce multidrug resistance protein 1 [19]. In the study, the inhibition of c-Jun phosphorylation was observed to reduce the Dox-induced multidrug resistance protein 1 expression and increase sensitivity of the small lung cancer cells to Dox. Overexpression of Hsp 27, the target protein of OGX-427, was found to decrease the intracellular level of topoisomerase II, which is important for sensitivity and initiation of apoptosis by Dox [20]. Specific inhibitors of c-un and Hsp 27 were found to increase chemosensitivity of cancer cells to Dox [21, 22]. Inhibition of c-Jun by Dz13 was shown to enhance the sensitivity of cancer cells to Dox treatment. A recent study reported that the reduced expression of Hsp 27 by resveratrol or short hairpin interfering RNA could sensitize MCF-7 breast cancer cells to Dox. Based on these findings, the higher in vivo antitumor activity of HMA nanoballs with co-treatment of Dox would be in part due to the enhanced chemosensitivity of KB cells to Dox by reduction of c-Jun and Hsp 27.

Moreover, the enhanced in vivo antitumor activity in the Dox/HMA nanoball co-treatment group could be attributable to the higher tumor accumulation of HMA revealed by molecular imaging (Fig. II-7). The improved stability of HMA nanoballs against DNase I could contribute to prolonging the circulation of DNA nanoballs in serum following intravenous administration. Our in vitro fluorescence microscopy and flow cytometry data revealed that the cellular uptake of HMA nanoballs and ASO significantly reduced after pre-treatment with free HA, supporting the possibility of enhanced tumor distribution of CD44-positive KB xenografted mice. Previously, to test whether HA microparticles enter tumor cells by CD44 receptor-mediated endocytosis in vivo, the tumor accumulation patterns of HA microparticles were compared between CD44-positive and CD44-negative tumor bearing mice [23]. Since MA nanoballs and HMA nanoballs differ in the surface charges, we can't exclude the contribution of negative surface charges of HMA nanoballs to the in vivo tumor distribution. Future study would be thus necessary to compare the distribution and antitumor activity of HMA nanoballs in CD44-positive and CD44-negative tumor-xenografted mice models.

# 5. References

[1]     Kole R, Krainer AR, Altman S. RNA therapeutics: beyond RNA interference and antisense oligonucleotides. Nature Rev Drug Discov. 2012; 11: 125-140.

[2]     Cai H, Santiago FS, Prado-Lourenco L, Wang B, Patrikakis M, Davenport MP. DNAzyme targeting c-jun suppresses skin cancer growth. Sci Transl Med. 2012; 4: 1-12.

[3]     Luvino D, Khiati S, Oumzil K, Rocchi P, Camplo M, Barthélémy P. Efficient delivery of therapeutic small nucleic acids to prostate cancer cells using ketal nucleoside lipid nanoparticles. J Control Release. 2013; 172: 954-961.

[4]     Hadaschik BA, Jackson J, Fazli L, Zoubeidi A, Burt HM, Gleave ME. Intravesically administered antisense oligonucleotides targeting heat-shock protein-27 inhibit the growth of non-muscle-invasive bladder cancer. BJU Int. 2008; 102: 610-616.

[5]     Tan ML, Dunstan DE, Friedhuber AM, Choong PF, Dass CR. A nanoparticulate system that enhances the efficacy of the tumoricide Dz13 when administered proximal to the lesion site. J Control Release. 2010; 144: 196-202.

[6]     Ballarín-González B, Howard KA. Polycation-based nanoparticle delivery of RNAi therapeutics: adverse effects and solutions. Adv Drug Deliv Rev. 2012; 64: 1717-1729.

[7]     Zhao W, Cui CH, Bose S, Guo D, Shen C, Wong WP. Bioinspired multivalent DNA network for capture and release of cells. Proc Natl Acad Sci U S A. 2012; 109: 19626-19631.

[8]     Hamblin GD, Carneiro KM, Fakhoury JF, Bujold KE, Sleiman HF. Rolling circle amplification-templated DNA nanotubes show increased stability and cell penetration ability. J Am Chem Soc. 2012; 134: 2888-2891.

[9]     Lee JB, Peng S, Yang D, Roh YH, Funabashi H, Park N. A mechanical metamaterial made from a DNA hydrogel. Nat Nanotechnol. 2012; 7: 816-820.

[10]    Lee JB, Hong J, Bonner DK, Poon Z, Hammond PT. Self-assembled RNA interference microsponges for efficient siRNA delivery. Nature Mater. 2012; 11: 316-322.

[11]    Zhang Z, Ali MM, Eckert MA, Kang DK, Chen YY, Sender LS. A polyvalent aptamer system for targeted drug delivery. Biomaterials. 2013; 34: 9728-9735.

[12]    Zöller M. CD44: can a cancer-initiating cell profit from an abundantly expressed molecule. Nature Rev Cancer. 2011; 11: 254-267.

[13]    Elahy M, Dass CR. Dz13: c-Jun downregulation and tumour cell death. Chem Biol Drug Des. 2011; 78: 909-912.

[14]    Baylot V, Andrieu C, Katsogiannou M, Taieb D, Garcia S, Giusiano S.

OGX-427 inhibits tumor progression and enhances gemcitabine chemotherapy in pancreatic cancer. Cell Death Dis. 2011; 2, e221.

[15] Jarvius J, Melin J, Go¨ransson J, Stenberg J, Fredriksson S, Gonzalez-Rey C, Bertilsson S. Digital quantification using amplified single molecule detection. Nature Methods. 2006; 3:725-727.

[16] Huang S, Chen Y. Polymeric sequence probe for single DNA detection. Anal Chem. 2011; 83: 7250-7254.

[17] Mok H, Park JW, Park TG. Antisense oligodeoxynucleotide-conjugated hyaluronic acid/protamine nanocomplexes for intracellular gene inhibition. Bioconjug Chem. 2007; 18: 1483-1489.

[18] Yao L, Wang Y, Xu S. Label-free microRNA detection based on exchange-induced remnant magnetization. Chem Commun. 2013; 49: 5183-5185.

[19] Shinoda C, Maruyama M, Fujishita T, Dohkan J, Oda H, Shinoda K. Doxorubicin induces expression of multidrug resistance-associated protein 1 in human small cell lung cancer cell lines by the c-jun N-terminal kinase pathway. Int J Cancer. 2005;117:21-31.

[20] Hansen RK, Parra I, Lemieux P, Oesterreich S, Hilsenbeck SG, Fuqua SA. Hsp27 overexpression inhibits doxorubicin-induced apoptosis in human breast cancer cells. Breast Cancer Res Treat. 1999; 56: 187–196.

[21] Dass CR, Khachigian LM, Choong PF. c-Jun knockdown sensitizes osteosarcoma to doxorubicin. Mol Cancer Ther. 2008; 7: 1909-1912.

[22] Díaz-Chávez J, Fonseca-Sánchez MA, Arechaga-Ocampo E, Flores-Pérez A, Palacios-Rodríguez Y, Domínguez-Gómez G. Proteomic profiling reveals that resveratrol inhibits HSP27 expression and sensitizes breast cancer cells to doxorubicin therapy. PLoS One. 2013; 8: e64378.

[23] Li S-D, Howell SB. CD44-targeted microparticles for delivery of cisplatin to peritoneal metastases. Mol Pharm. 2010; 7:280-290.

# Chapter III

# Polyaptamer DNA nanothread-anchored, reduced graphene oxide nanosheets for targeted delivery

# 1. Introduction

DNA aptamers have emerged as a potential targeting moiety for drug-delivery systems. DNA aptamers have been chemically conjugated [1] or physically complexed [2] to anti-cancer drugs. Carbon nanotubes have been physically adsorbed with DNA aptamers for anticancer drug delivery [3]. Notably, surface modification of nanoparticles with DNA aptamers has been reported to improve tumor accumulation [4,5]. Despite the ability of DNA aptamers to recognize specific cellular targets, the wide application of these targeting moieties to drug delivery has been hampered in part because their binding affinity is generally lower than that of antibodies [6].

Rolling circle amplification (RCA) is a recently developed molecular technique for amplifying single-stranded DNA (ssDNA) from a circular oligonucleotide, which acts as a template [7]. The amplified ssDNA contains repeating units of sequences complementary to the circular template. RCA has been applied to produce multivalent DNA aptamers for detection of small molecules [8] and target proteins [9,10]. Moreover, RCA-derived multivalent aptamers have been used to capture specific types of cells, showing improved binding affinities compared with monovalent DNA aptamers and antibodies in microfluidic devices [11].

Reduced graphene oxide (rGO) nanosheets have been studied as promising materials for anticancer drug delivery [12]. However, rGO nanosheets alone lack tumor-targeting ability. Conferring tumor-targeting ability to rGO nanosheets has been accomplished through modification with various molecules. Recently,

modification with cholesteryl hyaluronic acid has been reported to enhance the tumor distribution of rGO nanosheets [13]. However, using aptamers with high affinity and specificity represents an important strategy for enhancing the targeted delivery of rGO to tumor cells.

In this study, we hypothesized that coating rGO nanosheets with tumor-specific polyaptamer nanothreads would improve the tumor distribution and in vivo antitumor efficacy of anticancer drugs. To test this hypothesis, we generated tumor cell-specific polyaptamer nanothreads by RCA. Moreover, to enhance the anchoring capability of polyaptamers onto rGO, we introduced an oligonucleotide bridge sequence between repeating aptamer sequences. As a polyaptamer target, we chose protein tyrosine kinase 7 (PTK7), a biomarker for leukemia cells [14,15]. Here, we tested whether PTK7 polyaptamer nanothread-anchored rGO nanosheets could enhance the delivery of the anticancer drug, doxorubicin (Dox), to PTK7-overexpressing tumor tissues.

# 2. Materials and methods

## 2.1. Synthesis of polyaptamer nanothreads using RCA

PTK7 polyaptamer nanothreads without a bridge sequence (PN) or with a 22-mer T oligonucleotide (oligoT) bridge sequence (PNT) were synthesized using RCA reaction. Linear ssDNA templates of PN and PNT were hybridized to an RCA primer (Bioneer Corporation, Daejeon, Republic of Korea) designed to bind to 3' and 5' ends of the template. The sequence of the RCA primer for PN and PNT was 5'-CTG CGC CGC CGG GAA AAT ACT G-3'. The sequences of linear ssDNA templates were 5'-phosphate-CGG CGG CGC AGC AGT TAG ATT CTA ACC GTA CAG TAT TTT CC-3' for PN, and 5'-phosphate-CGG CGG CGC AGC AGT TAG ATA AAA AAA AAA AAA AAA AAA AAA TCT AAC CGT ACA GTA TTT TCC-3' for PNT. For some experiments, scrambled-sequence nanothreads containing an oligoT bridge sequence (SNT) were synthesized using an RCA reaction. The sequence of the RCA primer for SNT was 5'-ACT AGT CAG ATA TTA CTA TGA C-3', and the sequence of the linear ssDNA template for SNT was 5'-phosphate-ATC TGA CTA GTA TAT ACG GCA AAA AAA AAA AAA AAA AAA AAA GGT GCG CTC GGT CAT AGT AAT-3'. RCA templates for PN, PNT, and SNT are depicted in Fig. 1A. The RCA reaction was performed as described previously [16] with slight modifications. Briefly, 0.5 μM linear ssDNA template bearing a 5'-phosphate and 3'-hydroxyl group, and an RCA primer were first annealed in hybridization buffer (10 mM Tris-HCl pH 8.0, 1 mM EDTA, 100 mM NaCl) by heating to 95°C for 5 min and gradually cooling to room

temperature over 3 h. The complementary binding of an RCA primer to both ends of linear ssDNA allowed the formation of a circular ssDNA with a nick between 3' and 5' ends. The nick in the circular DNA was closed by adding 125 units/ml T4 DNA ligase (Thermo Scientific, Waltham, MA, USA) to 1 ml of reaction mixture and incubating at 4°C for 12 h. π29 DNA polymerase (100 units/ml; Thermo Scientific), RCA reaction buffer, and 2 mM dNTP (Intron Biotechnology, Seoul, Republic of Korea) were then added to the ligation mixture and incubated at 30°C for 5 min. Thereafter, π29 DNA polymerase was inactivated by heating at 70°C for 10 min, and the remaining dNTP was removed by size-exclusion chromatography using a PD-10 desalting column (GE Healthcare, Buckinghamshire, UK). The resulting RCA products were stored at 4°C until use.

## 2.2. Preparation of rGO nanosheets

Graphene oxide (GO) nanosheets were prepared from graphite by Hummer's method. In brief, 0.5 g graphite powder (Sigma-Aldrich, St. Louis, MO, USA), 3 g $KMnO_4$ (Sigma-Aldrich), and 0.5 g $NaNO_3$ (Sigma-Aldrich) were added to 23 ml cold $H_2SO_4$. After stirring for 1 h at 35°C, 46 ml water was added and the mixture was incubated at 90°C for 1 h. The reaction was stopped by adding 140 ml of water and 10 ml of 30 % $H_2O_2$. The product was purified by washing four times with centrifugation at $1600 \times$ g, first with 5 % HCl and then three times with triple-distilled water (TDW). The product was dispersed in TDW and sonicated for 2 h to exfoliate GO layers to GO nanosheets. Unexfoliated GO layers were

removed by centrifugation at $1600 \times g$ for 10 min. The supernatant was filtered through 0.2-µm polycarbonate membrane filters (Millipore Corp., Billerica, MA, USA) using an extruder (Northern Lipid, British Columbia, Canada).

rGO nanosheets were synthesized by reduction of GO nanosheets as previously described [13]. Briefly, 2 ml of GO nanosheets in water was mixed with 8 ml of water, 0.5 ml of ammonia solution (28 wt% in water; Junsei Chemical, Tokyo, Japan), and 5 µl of hydrazine monohydrate (64 % in water; Sigma-Aldrich). The mixture was stirred in a water bath at 80°C for 10 min. After cooling to room temperature, the remaining hydrazine and ammonia were eliminated by dialysis (MWCO 100K; Spectrum Laboratories, Inc., Rancho Dominguez, CA, USA) against TDW.

## 2.3. Anchoring nanothreads onto rGO nanosheets

PN-anchored rGO nanosheets (PNrGO), PNT-anchored rGO nanosheets (PNTrGO), and SNT-anchored rGO nanosheets (SNTrGO) were prepared by mixing nanothreads with the corresponding rGO nanosheets at a weight ratio of 0.5:1 (nanothread:nanosheet) and incubating at room temperature for 10 min. Anchoring efficiency of nanothreads was evaluated using a gel-retardation assay. Briefly, nanothreads and rGO nanosheet reaction mixtures were loaded onto a 0.8 % agarose gel containing 0.5 µg/mL ethidium bromide and electrophoresed for 30 min at 50 mV in Tris-borate-ethylenediamine-tetraacetic acid buffer. For comparison, free PN or PNT was loaded onto the gel. The migration of

rGO-unbound nanothreads was visualized using a Gel Doc System (Bio-Rad Lab., Hercules, CA, USA).

## 2.4. Characterization of nanothread-anchored rGO nanosheets

Nanothread-anchored rGO nanosheets were characterized by assessing morphology, size, zeta potential, and stability in aqueous solution. The morphology of PNT and PNTrGO was examined by transmission electron microscopy (TEM) using a JEM1010 transmission electron microscope (JEOL, Tokyo, Japan). The sizes of rGO nanosheets with or without nanothreads were measured using dynamic light scattering. The zeta potential values of rGO nanosheets with or without nanothreads were measured by laser Doppler microelectrophoresis at an angle of 22° using an ELS-8000 instrument (Photal, Osaka, Japan). The stability of rGO and PNTrGO was investigated by allowing a suspension of rGO or PNTrGO in phosphate-buffered saline (PBS; 50 mM, pH 7.4) to stand at room temperature, with periodic monitoring samples for the appearance of precipitates.

## 2.5. Loading of Dox onto rGO nanosheets

Dox was loaded onto rGO, SNTrGO, and PNTrGO by physical adsorption. Dox-loaded rGO (Dox/rGO), Dox-loaded SNTrGO (Dox/SNTrGO), and Dox-loaded PNTrGO (Dox/PNTrGO) were generated by adding Dox to the corresponding rGO nanosheets at a weight ratio of 1:5 (Dox:rGO nanosheets) and

incubating at room temperature for 10 min. Free Dox was then removed using a PD-10 desalting column (GE Healthcare). The extent of Dox loading onto various rGO nanosheets was determined by measuring the loss of Dox fluorescence at 485 nm caused by the quenching of rGO-adsorbed Dox using a fluorescence microplate reader (Gemini XS; Molecular Devices, Sunnyvale, CA, USA).

## 2.6. Preparation of fluorescent-marker–labeled rGO nanosheets

For cellular uptake studies and molecular imaging, PNTrGO and SNTrGO were labeled with cyanine 5.5 dye (Cy5.5) conjugated to the lipid, 1,2-distearoyl-*sn*-glycero-3-phosphoethanolamine-N-[amino(polyethylene glycol)-5000] (DSPE-PEG$_{5000}$-NH$_2$), containing PEG with a molecular weight of 5,000 (NOF Corporation, Tokyo, Japan). First, 4.5 mg of 1,2-DSPE-PEG$_{5000}$-NH$_2$ was dissolved in 2 ml of 0.1 M sodium bicarbonate buffer (pH 8.3), after which 1.0 mg of Cy5.5 NHS ester (Lumiprobe, Hallandale Beach, FL, USA) in 100 µl dimethyl sulfoxide was added with stirring for 4 h in the dark. The resulting 1,2-distearoyl-*sn*-glycero-3-phosphoethanolamine-N-[poly(ethylene glycol)$_{5000}$-N`]-cyanine 5.5 (DSPE-PEG$_{5000}$-Cy5.5) was purified using a self-packed Sephadex G15 column (GE Healthcare) and stored at 4°C until use. For labeling of various rGO nanosheets with DSPE-PEG$_{5000}$-Cy5.5, 100 µl of the corresponding rGO nanosheet solution (1 mg/ml) was mixed with 10 µl DSPE-PEG$_{5000}$-Cy5.5 (10 mg/ml). After sonication for 30 min, unbound DSPE-PEG$_{5000}$-Cy5.5 was removed by dialyzing the mixture (MWCO 1000K; Spectrum Laboratories, Inc.) against TDW for 24 h.

## 2.7. Cell culture

Human T-cell acute lymphoblastic leukemia (CCRF-CEM) cells and human Burkitt's lymphoma (Ramos) cells (Korean Cell Line Bank, Seoul, Republic of Korea) were cultured in RPMI-1640 medium (Welgene, Daegu, Republic of Korea) supplemented with 10 % fetal bovine serum and 100 units/ml penicillin plus 100 μg/ml streptomycin. The cells were grown at 37°C in a humidified 5 % $CO_2$ atmosphere.

## 2.8. PTK7 expression study

The expression of PTK7 on the surfaces of CCRF-CEM and Ramos cells was evaluated using flow cytometry. After harvesting, cells were incubated for 30 min at 4°C in cold PBS containing 3 % bovine serum albumin. Next, cells were washed and incubated for 30 min at 4°C with a monoclonal R-phycoerythrin (PE)-conjugated anti-PTK7 antibody (Miltenyi Biotec, Bergisch Gladbach, Germany) diluted 1:10 in cold PBS containing 2 % fetal bovine serum. Cells expressing PTK7 on the surface were identified by detection of fluorescent monoclonal antibodies.

## 2.9. Cellular uptake study

Cellular uptake of various rGO nanosheets was evaluated using confocal microscopy and flow cytometry. CCRF-CEM or Ramos cells were seeded onto 48-well plates at a density of $8 \times 10^4$ cells/well. After overnight incubation, cells were treated with DSPE-PEG$_{5000}$-Cy5.5–labeled rGO, SNTrGO or PNTrGO for 15

min, washed three times with PBS containing 2 % fetal bovine serum, and evaluated by confocal microscopy or flow cytometry. For flow cytometry, the cells were analyzed using a BD FACSCalibur system equipped with Cell Quest Pro software (BD Biosciences, San Jose, CA, USA). For confocal microscopy, the cells were transferred onto poly-L-lysine coated plates (BD Biosciences) and incubated for 1 h to allow cells to attach. Cells were then fixed with 4% paraformaldehyde in PBS for 15 min and stained with 4',6-diamidino-2-phenylindole dihydrochloride (DAPI). Cy5.5 fluorescence was observed using a confocal laser-scanning microscope (LSM 5 Exciter; Carl Zeiss, Inc., Jena, Germany).

## 2.10. In vitro anticancer activity assay

In vitro anticancer effects of Dox/rGO, Dox/SNTrGO, and Dox/PNTrGO were assessed against CCRF-CEM and Ramos cells. CCRF-CEM and Ramos cells were seeded into 48-well plates at a density of $4 \times 10^4$ cells/well. After overnight incubation, the cells were treated for 1 h with Dox/rGO, Dox/SNTrGO, or Dox/PNTrGO (2 μM Dox). The culture medium was then replaced, cells were incubated for an additional 24 h, and viability was measured using a Cell Counting Kit 8 (CCK-8; Dojindo Laboratories, Kumamoto, Japan) or live-cell staining assay (Molecular Probes, Eugene, OR, USA). For CCK-8 assays, 20 μl of CCK-8 solution was added to each well. After incubating for 30 min, the absorbance of the medium was measured colorimetrically at 450 nm using an enzyme-linked immunosorbent assay reader (Sunrise-Basic; TECAN, Mannedorf, Switzerland).

For live-cell staining assays, live cells were stained with calcein-AM after a 1 h treatment with Dox/rGO, Dox/SNTrGO, or Dox/PNTrGO.

## 2.11. In vivo molecular imaging

The biodistribution of DSPE-PEG$_{5000}$-Cy5.5-labeled SNTrGO and PNTrGO in mice was observed by molecular imaging. CCRF-CEM cells ($5 \times 10^6$) in a PBS solution containing 50 % matrigel (BD Biosciences) were subcutaneously inoculated into the dorsal right flank of 5-wk-old athymic nude mice (Orient Bio, Inc., Seongnam, Republic of Korea). After tumors had become established, DSPE-PEG$_{5000}$-Cy5.5-labeled, nanothread-anchored rGO nanosheets were intravenously administered into mice at a dose of 1 mg/kg. At various time points after intravenous injection, Cy5.5 signals of mice were scanned using an eXplore Opitx system (Advance Research Technologies Inc., Montreal, Canada) with a laser power of 25 mW and a count time of 0.3 s/point. A 670-nm pulsed-laser diode was used to excite Cy5.5. Long-wave fluorescence emission was detected with a fast photomultiplier tube (Hamamatsu Photonics, Hamamatsu, Japan) and a time-correlated single-photon counting system (Becker and Hickl GmbH, Berlin, Germany).

## 2.12. In vivo anti-tumor activity assay

The anti-tumor effects of Dox administered on various rGO nanosheets were tested using CCRF-CEM tumor-bearing mice. Five week-old athymic nude mice

were subcutaneously injected in the dorsal right flank with $5 \times 10^6$ CCRF-CEM cells in 50 % matrigel/PBS. When the tumors had grown to 150–180 mm$^3$, the mice were intravenously administered 3 mg/kg of Dox (15 mg/kg) as Dox/rGO, Dox/SNTrGO, or Dox/PNTrGO every other day for a total of three injections. Tumor size was measured in two dimensions using a slide caliper every other day, and tumor volume was calculated as a $\times$ b $\times$ b $\times$ 0.5, where a is the largest and b is the smallest dimension. For histopathological analyses, tumor tissues were excised and weighed on day 12. The sections were stained with anti-proliferating cell nuclear antigen (PCNA) antibody [17], and assayed using terminal deoxynucleotidyl transferase dUTP nick-end labeling (TUNEL) [17].

## 2.13. Statistics

All data were statistically analyzed using ANOVA with post hoc Student–Newman–Keuls test. SigmaStat software (version 3.5; Systat Software, Richmond, CA, USA) was used for analyses, and a p-value less than 0.05 was considered statistically significant.

# 3. Results

## 3.1. Effects of the oligoT bridge on nanothread anchoring to rGO

The effects of the oligoT bridge sequences on nanothread anchoring were tested by first producing PN, and PNT by the RCA reaction, as depicted in Fig. III-1A. Unlike the case for PN, a 22-mer A oligonucleotide sequence was included within the linear ssDNA template of PNT to produce oligoT in the RCA product. PN or PNT was mixed with rGO at a weight ratio of 0.5:1 to produce PNrGO or PNTrGO (Fig. III-1B). Gel retardation assays showed the presence of migrating unbound DNA nanothreads in PNrGO complexes but not in PNTrGO complexes (Fig. III-1C). These results indicate that the oligoT bridge sequences improved the ability of RCA nanothreads to anchor onto rGO nanosheets.

## 3.2. Physicochemical properties of PNTrGO

The morphology, size, zeta potential, and stability of PNTrGO in buffer were characterized. Transmission electron microscopy (TEM) showed that PNT alone exhibited a nanothread-like morphology (Fig. III-2A). TEM of PNTrGO revealed the presence of PNT anchored on rGO nanosheets (Fig. III-2B). Anchoring of PNT onto rGO nanosheets did not significantly affect the mean size of rGO nanosheets (Fig. III-2C), but did decrease zeta potential values (Fig. III-2D). Moreover, PNT coating enhanced the dispersion stability of rGO nanosheets in PBS (Fig. III-2E). Plain rGO nanosheets formed precipitates in PBS within 1 day. In contrast, PNTrGO remained stable in PBS for at least 7 days at room temperature.
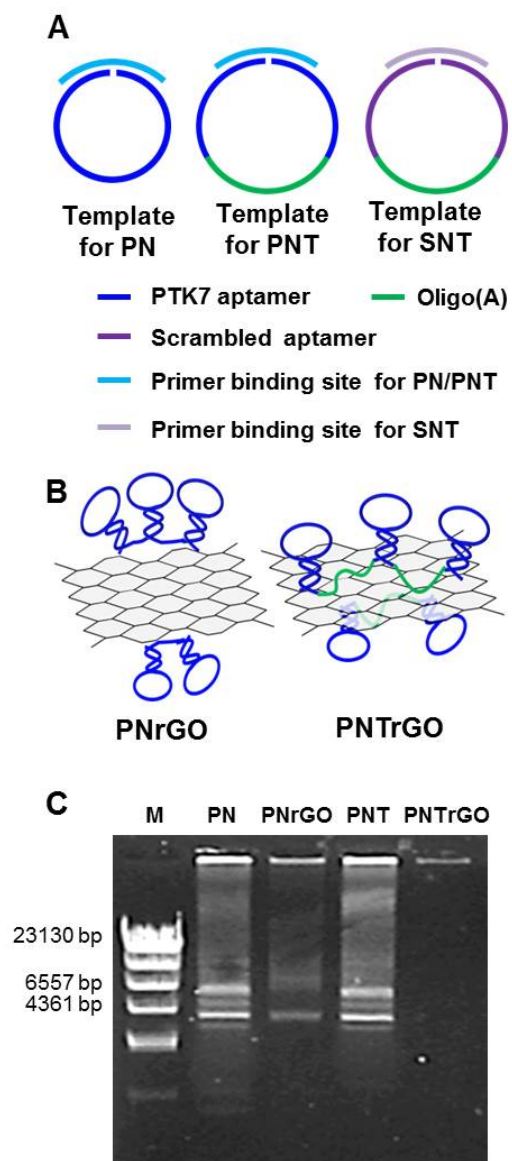
**Fig. III-1. Schematic illustration of PNrGO and PNTrGO nanosheets.**

(A) Templates of PN, PNT, and SNT for RCA. (B) Schematic representation of PNrGO and PNTrGO. (C) Complexation of rGO nanosheets with PN or PNT was analyzed by electrophoresis on 0.8 % (w/v) agarose gels.

Moreover, the loading efficiencies of Dox onto rGO (99.9 % ± 0.1 %) and PNTrGO (99.9 % ± 0.2 %) were not significantly different.

## 3.3. Enhanced cellular uptake of PNTrGO nanosheets in PTK7-positive cells

The cellular uptake of PNTrGO was enhanced in PTK7-positive cells, but not in the PTK7-negative cells. The dependence of PNTrGO uptake on PTK7 expression was tested by flow cytometry and fluorescence microscopy. Flow cytometry showed that PTK7 was not expressed on the surface of Ramos cells (Fig. III-3A), but was highly expressed on CCRF-CEM cells (Fig. III-3B), consistent with a previous report [18]. In PTK7-negative Ramos cells, the uptake of DSPE-PEG$_{5000}$-Cy5.5-labeled PNTrGO was not significantly different from that of DSPE-PEG$_{5000}$-Cy5.5-labeled SNTrGO, as determined by fluorescence microscopy (Fig. III-3C). In contrast, PTK7-positive CCRF-CEM cells showed greater uptake of fluorescent dye-labeled PNTrGO than fluorescent dye-labeled SNTrGO (Fig. III-3D). Consistent with these fluorescence microscopy data (Fig. III-3C, III-3D), flow cytometry revealed that notable cellular uptake of PNTrGO occurred in CCRF-CEM cells (Fig. III-3F), but not in Ramos cells (Fig. III-3E).

## 3.4. In vitro anticancer effects of Dox/PNTrGO nanosheets

Consistent with cellular uptake patterns, Dox/PNTrGO exhibited enhanced anticancer activity in PTK7-positive CCRF-CEM cells, but not in PTK7-negative Ramos cells (Fig. III-4A). In Ramos cells, the anticancer activity of Dox did not
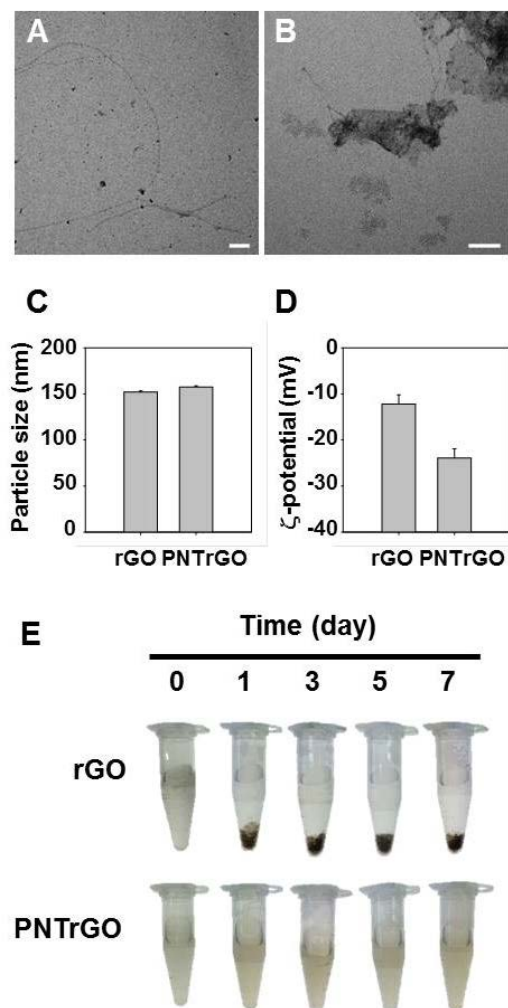
**Fig. III-2. Characterization of nanothread-anchored rGO nanosheets.**

The morphology of PNT (A) (scale bar, 200 nm) and PNTrGO nanosheets (B) (scale bar, 100 nm) was observed by TEM. (C) The sizes of rGO and PNTrGO were measured by dynamic light scattering. (D) Zeta potential values of rGO and PNTrGO were determined by laser Doppler microelectrophoresis at an angle of 22° using an ELS-8000 instrument. (E) The stability of rGO and PNTrGO was evaluated in PBS.
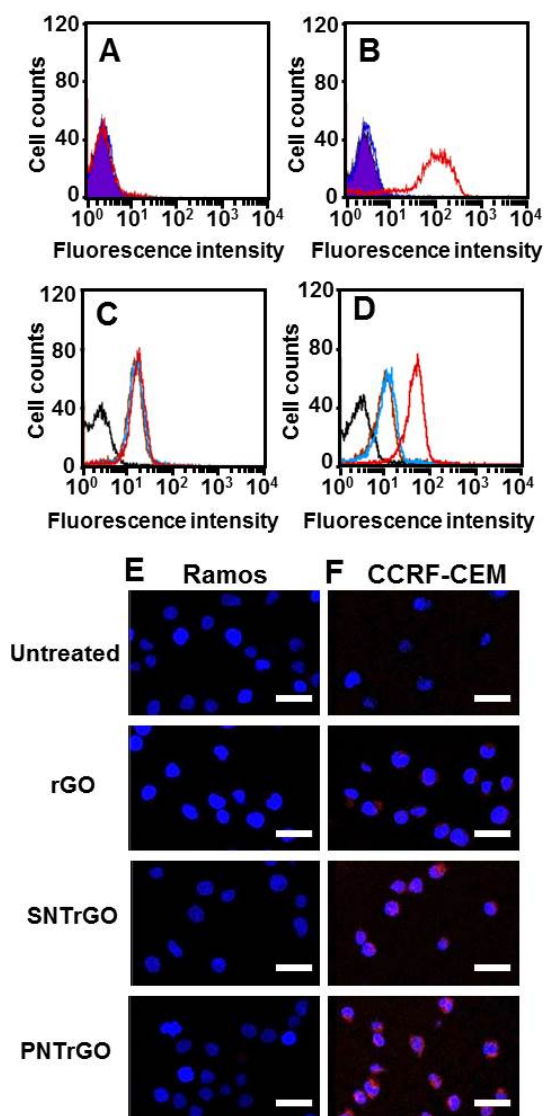
**Fig. III-3. Cellular uptake of various rGO nanosheets in PTK7-positive and -negative cells.**

Ramos cells (A) and CCRF-CEM cells (B) were stained with fluorescent anti-PTK7 antibody, and fluorescence-positive cells were measured by flow

cytometry. (C, E) Ramos cells were left untreated or were treated with rGO, SNTrGO, or PNTrGO. (D,F) CCRF-CEM cells were left untreated or were treated with rGO, SNTrGO, or PNTrGO. For detection of cellular uptake, rGO nanosheets were labeled with DSPE-PEG$_{5000}$-Cy5.5. After incubation for 15 min, cellular fluorescence was observed by flow cytometry (C,D), and confocal microscopy (E,F).

differ with respect to modification of rGO with PNT or SNT. In contrast, the anticancer activity of Dox toward CCRF-CEM cells was significantly higher following delivery with PNTrGO compared to delivery with rGO or SNTrGO (Fig. III-4B). Treatment of CCRF-CEM cells with Dox on PNTrGO reduced the viability of the cells to 43.1 % ± 9.2 % of that in control cells. Fluorescent dye-based live-cell staining assays revealed that the killing effect of Dox was greater when delivered by PNTrGO in CCRF-CEM cells (Fig. III-4D), but not in Ramos cells (Fig. III-4C).

## 3.5. Tumor tissue accumulation of nanothread-anchored rGO nanosheets

Following intravenous administration into CCRF-CEM tumor-bearing mice, fluorescent dye-labeled PNTrGO exhibited preferential tumor tissue accumulation. Compared with mice in fluorescent rGO and SNTrGO treatment groups, PNTrGO-treated mice showed tumor localization of fluorescence signal at 1 h (Fig. III-5A), 24 h (Fig. III-5B), and 48 h (Fig. III-5C). At 48 h, fluorescence intensity (photon count values) in tumor tissues was 2.3- and 2.5-fold higher in the PNTrGO-treated group than in groups treated with SNTrGO or rGO, respectively (Fig. III-5D).
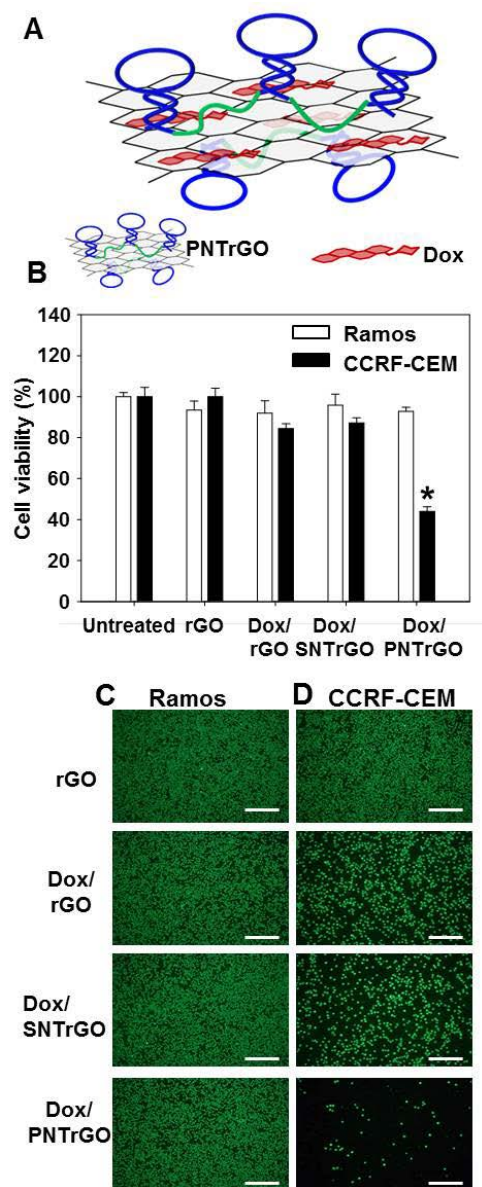
**Fig. III-4. In vitro anticancer effects of Dox delivered using nanothread-anchored rGO nanosheets .**

(A) A schematic depiction of Dox/PNTrGO is shown. (B) CCRF-CEM or Ramos

cells were treated with rGO, Dox/SNTrGO, or Dox/PNTrGO for 1 h. Untreated cells were used as a control. After incubation for an additional 24 h, the viability of cells was measured by CCK-8 assay. The results are the means ± SE of three independent experiments (*p < 0.05 compared to other groups; ANOVA and Student-Newman-Keuls test). Live Ramos cells (C) and CCRF-CEM cells (D) were stained with calcein-AM and observed by fluorescence microscopy. Scale bar, 250 μm.
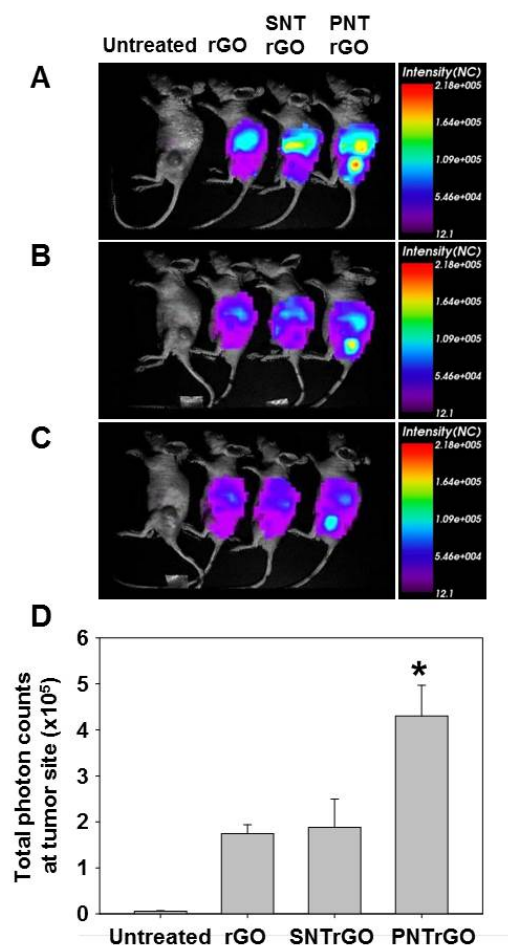
**Fig. III-5. Biodistribution of nanothread-anchored rGO nanosheets.**

CCRF-CEM tumor-bearing mice were intravenously injected with rGO, SNTrGO, or PNTrGO. DSPE-PEG$_{5000}$-Cy5.5 was used to label various rGO nanosheets for imaging. After 1 h (A), 24 h (B) and 48 h (C), the in vivo distribution of rGO nanosheets was visualized using a molecular imaging system. (D) Total photon counts in tumor sites relative to that in the untreated group were quantified 48 h post-dose using an in vivo imaging system (*p < 0.05 compared to other groups; ANOVA and Student-Newman-Keuls test).

## 3.6. In vivo anticancer effects of Dox delivered by various nanothread-anchored rGO nanosheets

Delivery of Dox by intravenous administration of Dox/PNTrGO produced the greatest antitumor effects against CCRF-CEM tumors in mice. On day 12, tumor volumes in mice treated with Dox/PNTrGO were significantly lower than those in mice treated with Dox/SNTrGO or Dox/rGO. In Dox/PNTrGO-treated mice, tumor volume was reduced to 23 % of that in untreated mice (Fig. III-6A), and tumor weight was reduced to 12 % (Fig. III-6B). In keeping with these tumor-growth–inhibitory effects (Fig. III-6A), PCNA staining showed that the proliferating cell population was lowest in tumor tissues of mice treated with Dox/PNTrGO (Fig. III-7A, III-7C). Moreover, TUNEL assays revealed that the apoptotic cell population in tumor tissues of mice treated with Dox/PNTrGO was 2.1- and 2.5-fold larger than that in Dox/SNTrGO-treated and Dox/rGO-treated groups, respectively (Fig. III-7B, III-7D).
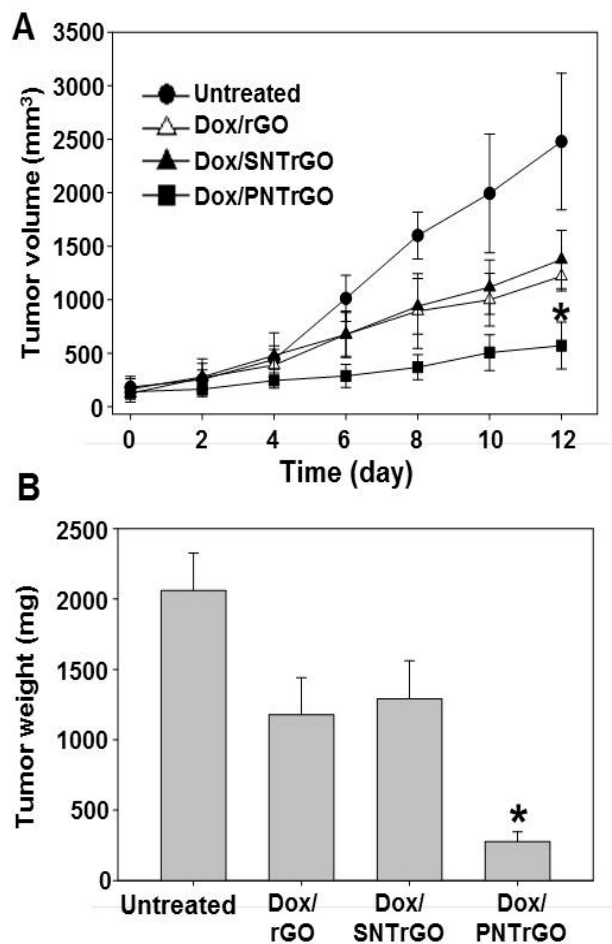
**Fig. III-6. In vivo antitumor effects of Dox on nanothread-anchored rGO nanosheets.**

(A) CCRF-CEM tumor-bearing mice were treated three times by intravenous administration of 3 mg/kg of Dox on rGO, SNTrGO, or PNTrGO every other day (B) On day 12, tumor tissues were excised and weighed (n = 4; *p < 0.05 compared to other groups; ANOVA and Student-Newman-Keuls test).
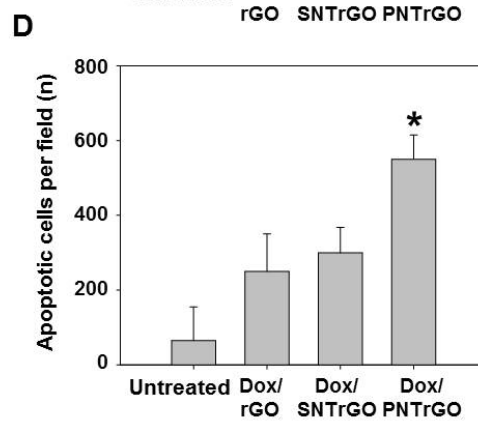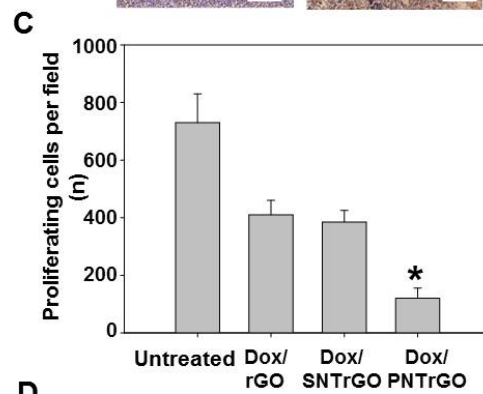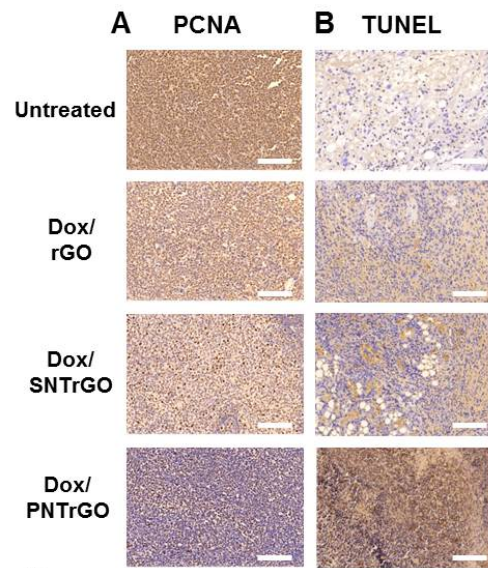
**Fig. III-7. Immunohistochemistry of tumor tissues.**

Tumor tissues excised on day 12 after tumor inoculation were analyzed by immunostaining for PCNA (A) and by performing TUNEL assays (B). The numbers of PCNA-immunostained proliferating cells (C) and TUNEL-labeled apoptotic cells (D) in tumor tissue sections were determined (n = 4; *p < 0.05 compared to other groups; ANOVA and Student-Newman-Keuls test). Scale bar, 200 μm.

# 4. Discussion

Here, we demonstrated that PNTrGO nanosheets can be used for targeted delivery of anti-cancer drugs to PTK7-positive tumor tissues. The introduction of an oligoT bridge between aptamer sequences increased the ability of RCA nanothreads to anchor onto rGO nanosheets. Surface modification of rGO with PNT resulted in improved cellular uptake into PTK7-positive tumor cells lines and enhanced tumor tissue accumulation compared to SNTrGO nanosheets. Moreover, systemic administration of Dox using PNTrGO enhanced the antitumor effects in mice bearing PTK7-positive tumors.

TEM analyses revealed that PTK7-targeting polyaptamer sequences produced by RCA of ssDNA templates exhibited a nanothread-like morphology (Fig. III-2A). In RCA reactions, π29 DNA polymerase replicates circular DNA templates over many rounds to yield products typically tens of thousands of nucleotides long [10,19].

We observed that PNT showed a greater ability to bind rGO nanosheets than PN (Fig. III-1C). The single-stranded oligoT bridge between each PTK7 aptamer sequence may serve as an rGO-anchoring unit. It has been reported that graphene-based nanosheets are capable of adsorbing ssDNA via π-π stacking interactions between the ring structures in the nucleobases. Graphene-based nanosheets are known to have lower affinity for dsDNA or ssDNA with secondary and tertiary structure owing to shielding of nucleobases within the negatively charged phosphate backbone [20]. Since PTK7 aptamers possess a specific tertiary

structure that enables binding to PTK7, the affinity of PTK7 aptamer alone for rGO nanosheets might be expected to be lower than that of oligoT sequences. Consistent with this supposition, the addition of oligoT sequence increased the binding of nanothreads onto rGO nanosheets.

In addition to conferring PTK7-recognition ability, PNT on rGO could serve as a dispersion stabilizer of rGO nanosheets in PBS. Poor solubility and aggregation in physiological buffers in the presence of salts have been linked to safety concerns surrounding the use of graphene-based nanosheets. Chemical modifications of surfaces with hydrophilic polymers such as PEG have been used to enhance the stability of graphene-based nanosheets [21]. In this latter study, adsorption of DNA onto the surface of GO nanosheets was reported to increase stability in aqueous solutions for several months, completely preventing aggregation [22]. The enhanced stability of PNTrGO in PBS observed here might offer greater stability of rGO nanosheets in serum after systemic administration.

PNTrGO was taken up by CCRF-CEM cells with greater efficiency than SNTrGO (Fig. III-3F). This enhanced cellular uptake of PNTrGO is attributable to the expression of PTK7 on CCRF-CEM cells (Fig. III-3B), as evidenced by the diminished uptake of PNTrGO by PTK7-negative Ramos cells (Fig. III-3A). Moreover, upon binding ligands, namely the PTK7-targeting DNA aptamer sgc8, PTK7 has been shown to undergo endocytosis [18], a crucial mechanism in the cellular entry of nanocarriers.

To visualize the cellular uptake and in vivo fate of PNTrGO, we labeled the surfaces of PNTrGO with the fluorescent lipid dye, DSPE-PEG$_{5000}$-Cy5.5, which

adheres to the surfaces of rGO through hydrophobic interaction. Although graphene-based nanosheets exert a strong quenching effect on fluorescent probes, providing a sufficient distance from the surfaces of nanosheets can prevent fluorescence resonance energy transfer, thereby avoiding quenching. The relatively long PEG spacer in the DSPE-PEG$_{5000}$-Cy5.5 fluorescent lipid used here thus minimizes quenching upon adsorption to rGO surfaces.

Our in vivo molecular imaging data revealed that PNTrGO nanosheets exhibited enhanced tumor distribution (Fig. III-5D). The greater tumor distribution of PNTrGO implies that PNT was not degraded in the systemic circulation, and was capable of recognizing and binding PTK7-expressing tumor cells upon arrival in tumor tissues. The adsorption of PNT onto rGO may have contributed to the enhanced stability of PNT against the nuclease-rich in vivo environment. Indeed, graphene-based nanosheets have been previously reported to protect DNA adsorbed onto the graphene surface from nuclease digestion [23]. Specifically, this latter study showed that a molecular beacon adsorbed onto graphene oxide surfaces was protected from enzymatic cleavage and was delivered to targeted cells, resulting in visualization and detection of intracellular survivin mRNA [24]. Another study reported enhanced nuclease resistance of ATP aptamers upon adsorption to graphene oxide nanosheets.

The anti-cancer effects of Dox were greatest both in vitro and in vivo after delivery using PNTrGO (Figs. III-4 and III-6). Although the release profile of Dox from graphene-based nanosheets is not fully characterized, it has been reported that release of Dox loaded onto pegylated GO nanosheets is facilitated in an acidic

solution (pH 5.5), and is reduced at more neutral pH values (pH 7.4) [25]. Accordingly, as suggested by the results of a previous study , after endocytosis via PTK7, Dox on PNTrGO could be released in acidic endosomes and diffuse out to the nucleus.

# 5. References

[1]     Huang YF, Chang HT, Tan W. Cancer cell targeting using multiple aptamers conjugated on nanorods. Anal Chem. 2008; 80: 567-572.

[2]     Bagalkot V, Zhang L, Levy-Nissenbaum E, Jon S, Kantoff PW, Langer R. Quantum dot-aptamer conjugates for synchronous cancer imaging, therapy, and sensing of drug delivery based on bi-fluorescence resonance energy transfer. Nano Lett. 2007; 7: 3065-3070.

[3]     Taghdisi SM, Lavaee P, Ramezani M, Abnous K. Reversible targeting and controlled release delivery of daunorubicin to cancer cells by aptamer-wrapped carbon nanotubes. Eur J Pharm Biopharm. 2011; 77: 200-206.

[4]     Cao Z, Tong R, Mishra A, Xu W, Wong GC, Cheng J. Reversible cell-specific drug delivery with aptamer-functionalized liposomes. Angew Chem Int Edit. 2009; 48: 6494-6498.

[5]     Kang H, O'Donoghue MB, Liu H, Tan W. A liposome-based nanostructure for aptamer directed delivery. Chem Commun. 2010; 46: 249-251.

[6]     McNamara JO, Kolonias D, Pastor F, Mittler RS, Chen L, Giangrande PH. Multivalent 4-1BB binding aptamers costimulate CD8+ T cells and inhibit tumor growth in mice. J Clin Invest. 2008; 118: 376-386.

[7]     Ali MM, Li F, Zhang Z, Zhang K, Kang DK, Ankrum JA. Rolling circle amplification: a versatile tool for chemical biology, materials science and medicine Chem Soc Rev. 2014; 43: 3324-3341.

[8]     Cho EJ, Yang L, Levy M, Ellington AD. Using a deoxyribozyme ligase and rolling circle amplification to detect a non-nucleic acid analyte, ATP. J Am ChemSoc. 2005; 127: 2022-2023.

[9]     Yang L, Fung CW, Cho EJ, Ellington AD. Real-time rolling circle amplification for protein detection. Anal Chem. 2007; 79: 3320-3329.

[10]    Cheglakov Z, Weizmann Y, Braunschweig AB, Wilner OI, Willner I. Increasing the complexity of periodic protein nanostructures by the rolling-circle-amplified synthesis of aptamers. Angew Chem Int Edit. 2008; 47:126-130.

[11]    Zhao W, Cui CH, Bose S, Guo D, Shen C, Wong WP. Bioinspired multivalent DNA network for capture and release of cells. Proc Natl Acad Sci USA. 2012; 109: 19626-19631.

[12]    Liu J, Li Y, Lib J, Deng Z. Noncovalent DNA decorations of graphene oxide and reduced graphene oxide toward water-soluble metal–carbon hybrid nanostructures via self-assembly. J Mater Chem. 2010; 20: 900-906.

[13]  Miao W, Shim G, Kang CM, Lee S, Choe YS, Choi HG. Cholesteryl hyaluronic acid-coated, reduced graphene oxide nanosheets for anti-cancer drug delivery. Biomaterials. 2013; 34: 9638-9647.

[14]  Shangguan D, Li Y, Tang Z, Cao ZC, Chen HW, Mallikaratchy P. Aptamers evolved from live cells as effective molecular probes for cancer study. Proc Natl Acad Sci USA. 2006; 103: 11838-11843.

[15]  Shangguan D, Cao Z, Meng L, Mallikaratchy P, Sefah K, Wang H. Cell-specific aptamer probes for membrane protein elucidation in cancer cells. J Proteome Res. 2008; 7: 2133-2139.

[16]  Beyer S, Nickels P, Simmel FC. Periodic DNA nanotemplates synthesized by rolling circle amplification. Nano Lett. 2005; 5: 719-722.

[17]  Zhang Y, Schwerbrock NMJ, Rogers AB, Kim WY, Huang L. Codelivery of VEGF siRNA and gemcitabine monophosphate in a single nanoparticle formulation for effective treatment of NSCLC. Mol Ther. 2013; 21: 1559-1569.

[18]  Xiao Z, Shangguan D, Cao Z, Fang X, Tan W. Cell-specific internalization study of an aptamer from whole cell selection. Chemistry. 2008; 14: 1769-1775.

[19] Lee JB, Peng S, Yang D, Roh YH, Funabashi H, Park N. A mechanical metamaterial made from a DNA hydrogel. Nat Nanotechnol. 2012; 7: 816-820.

[20] He BS, Song B, Li D, Zhu C, Qi W, Wen Y. A graphene nanoprobe for rapid, sensitive, and multicolor fluorescent DNA analysis. Adv Funct Mater. 2010; 20:453-459.

[21] Zhu G, Zheng J, Song E, Donovan M, Zhang K, Liu C. Self-assembled, aptamer-tethered DNA nanotrains for targeted transport of molecular drugs in cancer theranostics. Proc Natl Acad Sci USA. 2013; 110:7998-8003.

[22] Lu CH, Zhu CL, Li J, Liu JJ, Chen X, Yang HH. Using graphene to protect DNA from cleavage during cellular delivery. Chem Commun. 2010; 46:3116-3118.

[23] Wang Y, Li Z, Hu D, Lin CT, Li J, Lin Y. Aptamer/graphene oxide nanocomplex for in situ molecular probing in living cells. J Am Chem Soc. 2010;132: 9274-9276.

[24] Sun X, Liu Z, Welsher K, Robinson JT, Goodwin A, Zaric S. Nano-graphene oxide for cellular imaging and drug delivery. Nano Res. 2008; 1: 203-212.

[25] Estrella V, Chen T, Lloyd M, Wojtkowiak J, Cornnell HH, Ibrahim-Hashim A. Acidity generated by the tumor microenvironment drives local invasion. Cancer Res. 2013; 73:1524-1535.

**Chapter IV**


**Polyaptamer DNA and graphene oxide hybrid hydrogel**

# 1. Introduction

DNA has recently emerged as a biomaterial for drug-delivery systems. One specific class of drug-delivery systems is three-dimensional hydrogels. Although these hydrogels have attracted interest for possible biological and medical applications, the development of DNA-based hydrogels with designable properties is still in its early stages. DNA hydrogels are natural, biocompatible and biodegradable [1]. DNA hydrogels have been studied as drug-delivery [2] and gene-delivery [3] vehicles, and as biosensors [4,5].

DNA hydrogels have been prepared by hybridization of nucleic acid units with chemical or DNA cross-linkers. Ethylene glycol diglycidyl ether [6,7] and azobenzene [8] have been used as DNA hydrogel chemical cross-linkers. DNA molecules with sticky ends also serve as cross-linkers to form three-dimensional DNA hydrogels [9,10].

Until now, little attention has been paid to the functionality and drug specificity of DNA molecules used for DNA hydrogel matrices. Recently, CpG sequence-containing DNA hydrogels were studied for their ability to confer immunomodulation [2]. A previous study reported DNA hydrogels designed to deliver doxorubicin [11]. In the study, drug loading onto DNA hydrogels was produced by non-specific electrostatic interactions between the positively charged drug molecule and negatively charged DNA, which may limit the application of hydrogels to positively charged drugs.

In this study, we propose an injectable DNA hybrid hydrogel using single-stranded DNA (ssDNA) and polyaptamer sequences as a drug-specific hydrogel matrix and graphene oxide (GO) nanosheets as a cross-linker. GO interacts with ssDNA, but not with double-stranded DNA [12,13], a property we exploited in selecting GO as a cross-linker in ssDNA-sequence–containing hydrogels. Drug-specificity was provided to DNA hydrogel matrices by introducing a drug-specific polyaptamer sequence between GO-binding ssDNA. Drug-specific polyaptamer and GO-binding ssDNA sequences were obtained by rolling-circle amplification (RCA), and then cross-linked in the presence of GO. Here, we report the construction, rheology, and drug specificity of GO-crosslinked polyaptamer (GO-PA) hybrid hydrogels using kanamycin as a model drug.

# 2. Materials and methods

## 2.1. Synthesis of rGO nanosheets

GO nanosheets were prepared from graphite powder according to a modification of Hummer's method, as described previously [14]. In brief, graphite powder (0.5 g; Sigma-Aldrich, St. Louis, MO, USA) was added to cold $H_2SO_4$ (23 ml) and stirred on ice, after which $KMnO_4$ (3 g) and $NaNO_3$ (0.5 g) were added slowly. Following continuous stirring for 1 h at 35°C, 46 ml of triple-distilled water (TDW) was added and the solution was incubated for 1 h at 90°C. The reaction was stopped by adding 140 ml TDW and 10 ml 30 % $H_2O_2$. The product was thoroughly washed and purified by repeated centrifugation of the resulting mixture. The purified product was suspended in TDW and sonicated for 2 h to exfoliate the agglomerated GO layers into single GO nanosheets. Unexfoliated GO was removed by centrifugation, and the supernatant containing GO nanosheets was collected.

## 2.2. Preparation of circular ssDNA template for RCA

Circular DNA templates for RCA were prepared using a 5'-phosphorylated linear ssDNA template. The phosphorylated linear ssDNA template was composed of an RCA primer-complementary sequence for circle formation, a GO binding 12-mer oligo A sequence, and a kanamycin-binding aptamer to provide drug specificity. The sequence of the primer was 5'-GTA CGT GCT AGC CGA TAT GCC T-3', and the sequence of the polyaptamer template was 5'-phosphate-ATC

GGC TAG CAC GTA CAG AAC TAA AAA AAA AAA A<u>GT CGG CTT AGC CTC AAC CCC C</u>AA GGC AAA AAG GCA T-3', where the underlined 21-mer is an aptamer sequence for kanamycin [15]. In some experiments, a control RCA template in which the kanamycin-specific aptamer sequence was replaced with a scrambled random sequence with the same number of bases (5'-phosphate-ATC GGC TAG CAC GTA CAG AAC TAA AAA AAA AAA AGT GCG CTC GGT CAT AGT ACG GAA GGC AAA AAG GCA T-3') was used. In experiments designed to test the role of 12-mer oligo A, a polyaptamer template lacking the 12-mer oligo A (5'-phosphate-ATC GGC TAG CAC GTA CAG AAC T<u>GT CGG CTT AGC CTC AAC CCC C</u>AA GGC AAA AAG GCA T-3') was used. The linear ssDNA template and circular-form–inducing RCA primers were from Bioneer Co. (Daejeon, Republic of Korea). For RCA, 5'-phosphorylated linear ssDNA template (0.5 μM) was mixed with 0.5 μM of its corresponding primer in 1 ml of hybridization buffer (10 mM Tris-HCl, 1 mM EDTA, 100 mM NaCl, pH 8.0). The solution was thoroughly vortexed, heated for 5 min at 95°C, and then allowed to cool slowly to 30°C over a 3 h period. The primer-hybridized circular template (50 nM) was reacted with 25 μl (equivalent to 125 Weiss units) of T4 DNA ligase (Thermo Fisher Scientific Inc., Waltham, MA, USA) in 1 ml of T4 DNA ligase reaction buffer for 12 h at 4°C. The solution was then incubated for 10 min at 70°C to inactivate the ligase and stored at -20°C until use.

## 2.3. RCA-mediated synthesis of GO-PA hybrid hydrogels

Kanamycin-specific polyaptamer-based hydrogels with GO as a crosslinker

were synthesized by amplifying circular RCA templates in the presence of GO nanosheets. Circular ssDNA template (10 nM) containing a 21-bp kanamycin-specific aptamer sequence or scrambled DNA sequence was treated with a 10 mM dNTP mix (Applied Biosystems, Seoul, Republic of Korea) and $\pi$29 DNA polymerase (volume equivalent to 1 % of the total reaction volume) in 1.2 ml of $\pi$29 DNA polymerase reaction buffer (Thermo Fisher Scientific Inc.). The mixture was vortexed, and the RCA reaction was allowed to proceed at 30°C for 0.5 h. GO (200 μg) was then added and, after vortexing the mixture for 30 s, the RCA reaction was continued for 11.5 h. The resulting GO-PA hybrid hydrogels or GO-crosslinked scrambled (GO-SC) hydrogels were kept at room temperature until use.

## 2.4. Scanning electron microscopy

The morphology of GO-PA hybrid hydrogels was observed by scanning electron microscopy (SEM). GO-SC or GO-PA hydrogels were spray-coated with Au/Pd. The coated samples were then placed onto a 12-mm diameter copper grid (FESEM Finder grid; Ted Pella Inc., Redding, CA, USA), and SEM images were obtained using a Field-Emission SEM/FIB (focused ion beam) system (Carl Zeiss Inc., Thornwood, NY, USA).

## 2.5. Measurement of GO-PA hybrid hydrogel swelling ratios

The swelling ratio of hydrogels was calculated from their water uptake capacity. GO-PA hybrid hydrogel was dehydrated by freeze-drying (FreeZone 2.5; Labconco,

MO, USA). The dehydrated hydrogel was then immersed in 2 ml of TDW and incubated at 37°C. At predetermined time points, the hydrogel was removed, blotted with tissue paper, and weighed. The swelling ratio of the hydrogel was calculated from the following equation: Swelling ratio (%) = $[(W_s - W_i)/W_i] \times 100$, where $W_i$ represents the weight of the dehydrated hydrogel and $W_s$ the weight of the rehydrated hydrogel.

## 2.6. Rheology and X-ray diffraction pattern measurements

A rotational rheometer (DHR-1; TA Instruments Ltd., DE, USA) was used to measure rheological properties of the GO-PA hybrid hydrogel. The hydrogel was placed on the plate of the rheometer, and shear storage and loss modulus were measured using dynamic frequency sweeping mode with strain fixed at 5 %. The X-ray diffraction (XRD) patterns of dried plain GO and GO-PA hybrid hydrogels were analyzed using a high resolution X-ray diffractometer (D8 Discover; Bruker Corp., Billerica, MA, USA).

## 2.7. Loading of kanamycin into GO-PA hybrid hydrogels

Kanamycin was loaded into GO-PA hydrogels through aptamer-target specific interactions. Hydrogels (1.8 mg) were immersed in 1 ml of kanamycin sulfate (100 µg/ml) in TDW for 10 min. Hydrogels were then transferred to a tube containing 1 ml of fresh TDW and the tube was inverted several times to remove any kanamycin that had transiently adhered through non-specific interactions. Kanamycin loading capacity of the hydrogel was quantified by measuring the

fluorescence of fluorescein isothiocyanate (FITC)-conjugated kanamycin after dialysis against TDW using a 1000-Da dialysis membrane (Spectra/Por 7 Dialysis Membrane; Spectrum Labs, CA, USA).

In some experiments, fluorescent kanamycin (F-Kan) or fluorescent gentamicin (F-Gen) was loaded into GO-PA hydrogels to produce F-Kan-loaded GO-PA (F-Kan/GO-PA) or F-Gen-loaded GO-PA (F-Gen/GO-PA) hybrid hydrogels. Fluorescent antibiotics were synthesized by mixing 43.44 mg FITC (Sigma Aldrich Co.) with 130 mg kanamycin sulfate salt (Duchefa Biochemie, Haarlem, Netherlands) or 130 mg gentamicin sulfate salt (Duchefa Biochemie) in a solution of 0.5 ml triethylamine and 10 ml dimethyl formamide (both from Sigma-Aldrich Co.). The mixture was incubated for 16 h with stirring. Thereafter, the solvent was evaporated, and the resulting powder was washed twice with 10 ml methanol and then with 10 ml acetone. The purified powder was dried by vacuum evaporation and dissolved in TDW to yield F-Kan or F-Gen solutions. In addition to quantitative evaluation, drug loading was qualitatively demonstrated by imaging hydrogels using the BioRad GelDoc XR system (BioRad, Hercules, CA, USA) in Trans-UV mode.

## 2.8. Antibacterial efficacy of Kan/GO-PA hybrid hydrogels

The antibacterial effects of Kan/GO-PA hybrid hydrogels against both gram-positive and gram-negative bacteria were investigated. Gram-negative *Enterobacteriaceae* (*Escherichia coli*) and gram-positive *Staphylococcus aureus* were obtained from American Type Culture Collection (Manassas, VA, USA). *E.*

*coli* was grown in nutrient broth (NB) and *S. aureus* in trypticase soy broth (TSB) medium, as recommended by the supplier. The selected assay method was the colony formation assay. Briefly, 100 µl of *E. coli* or *S. aureus*, each at an optical density at 600 nm ($OD_{600}$) of 0.3, were diluted with 100 µl of NB and TSB, respectively. Kan/GO-PA hydrogels were then incubated in bacterial solutions at 37°C for 1 h with stirring. Stirring was then halted and solutions were left undisturbed for 5 min. Once the hydrogel had settled to the bottom of the tube, 200 µl of *E. coli* and *S. aureus* solutions was inoculated onto NB and TSB agar plates, respectively, and incubated overnight at 37°C. The next day, the plates were imaged using Epi-white exposure, and the number of colonies on each plate was determined using the BioRad GelDoc XR system.

## 2.9. In vivo imaging of GO-PA hybrid hydrogel

For in vivo molecular imaging, F-Kan/GO-PA hydrogel (1.8 mg) was injected subcutaneously into the right flank of a shaved Balb/c mouse (Orientbio Inc., Seongnam, Republic of Korea) using a 1 ml insulin syringe (BD Ultra-fine II insulin syringes; Becton Dickinson and Company, Franklin Lakes, NJ, USA). Mice were shaved to eliminate interference with fluorescence detection caused by hairs. Fluorescence intensity emanating from the injected hydrogel was detected at predetermined time points with an Optix molecular imaging system (Advance Research Technologies Inc. Montreal, Canada) at a wavelength of 485 nm and an exposure time of 12 ns.

# 3. Results

## 3.1. Construction of GO-PA hybrid hydrogels

GO-PA hybrid hydrogels were constructed using a DNA hydrogel matrix with GO as crosslinker. As depicted in Figure IV-1, the RCA template was composed of a circularizing primer-binding sequence, a GO-binding 12-mer oligo A sequence, and 21-mer kanamycin-binding aptamer sequence. The GO-binding 12-mer oligo A sequence was introduced to exploit the ssDNA-binding property of GO nanosheets. GO nanosheets were added partway through the RCA reaction (30 min after RCA initiation) to ensure that the ssDNA produced by RCA would be adsorbed onto GO nanosheets concomitant with continuous production of RCA products. In the presence of GO nanosheets, RCA scrambled or polyaptamer template containing the 12-mer oligo A sequence formed a light brown GO-PA hybrid gel after the RCA reaction.

## 3.2. Characterization of GO-PA hybrid hydrogels

GO-PA hybrid hydrogels were characterized with respect to morphology, X-ray diffraction pattern, swelling behavior, and rheologic properties. The topology of GO-PA hydrogels was examined by SEM, which showed that, whereas the surfaces of GO nanosheets were relatively smooth (Fig. IV-2), those of GO-PA hybrid hydrogels was rough and ruffled (Fig. IV-2B). Notably, an enlarged image of GO-PA hybrid hydrogels (Fig. IV-2C) showed pores spread throughout the structure. X-ray diffraction (XRD) patterns differed between GO nanosheets and
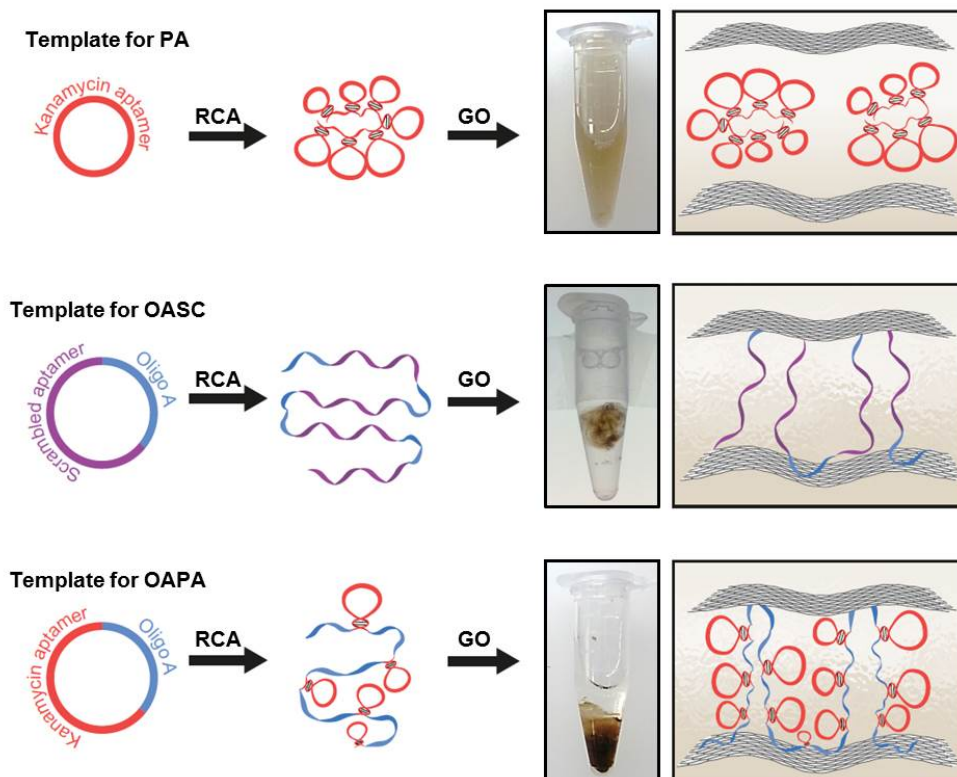
**Fig. IV-1. Construction of GO-PA hybrid hydrogels.**

Schematic mechanism of GO-PA hybrid hydrogel formation through a single-step RCA reaction. The compositions of RCA templates for kanamycin-specific polyaptamer with or without a 12-mer oligo A sequence, or scrambled polyaptamer with a 12-mer oligo A sequence.
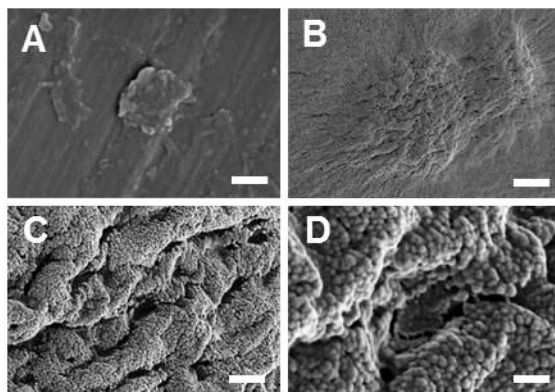
**Fig. IV-2. Morphology of GO-PA hybrid hydrogels.**

SEM images of GO nanosheets alone (A) and GO-PA hybrid hydrogels (B, C, D) of different magnifications. Scale bars = 100 nm (A), 2 μm (B), 400 nm (C), and 100 nm (D).

GO-PA hybrid hydrogels. The distinctive XRD peak of GO nanosheets at 9.5°
disappeared in the XRD pattern of GO-PA hybrid hydrogels (Fig. IV-3A). The
swelling ratio of dried GO-PA hydrogel in TDW increased over time, reaching a
maximum at 2 h (Fig. IV-3B). The hydrogel was capable of swelling up to 700%,
whereas the dried RCA product of polyaptamer template containing the 12-mer
oligo A sequence showed no water uptake. With respect to the dynamic rheological
behavior, shear storage (G′) values of GO-PA hydrogels were higher than loss
modulus (G″) values over a range from 0.01 to 10 Hz (Fig. IV-3C).

### 3.3. Kanamycin-specific loading into GO-PA hydrogels

The proposed GO-PA hydrogels could specifically entrap kanamycin in the
hydrogel matrix, as depicted in Figure IV-4A. Estimates of drug loading efficiency,
determined by monitoring the fluorescence intensity of F-Kan-loaded hydrogels,
confirmed this. In contrast to GO-SC hydrogels, which showed a 1.5 % F-Kan
loading efficiency (Fig. IV-4B), GO-PA hydrogels showed a F-Kan loading
efficiency of 58.0 %—38-fold higher than that of GO-SC hydrogels. Both
hydrogels were indistinguishable under the naked eye, but under 320 nm UV light,
only F-Kan/GO-PA hydrogels showed F-Kan fluorescence (Fig. IV-4C). In contrast,
the loading efficiencies of F-Gen were 1.2 % for GO-SC and 1.3 % for GP-PA
hydrogels (Fig. IV-4B), and F-Gen/GO-PA hydrogels exhibited little fluorescence
upon UV illumination (Fig. IV-4C).
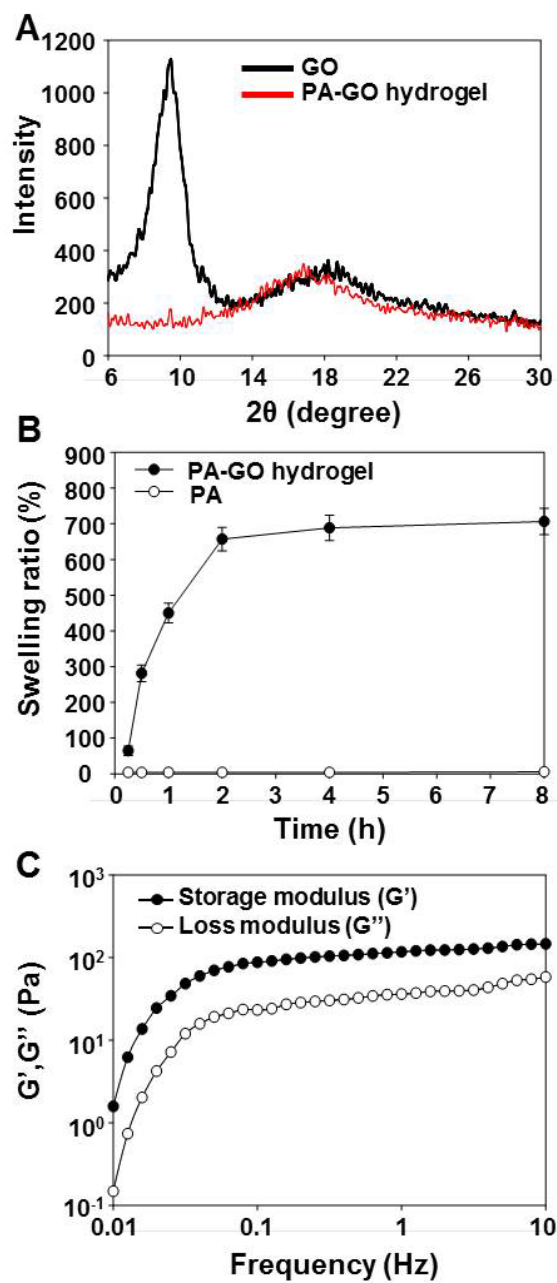
**Fig. IV-3. Physicochemical characterization of GO-PA hybrid hydrogels.**

(A) XRD patterns of plain GO nanosheets and GO-PA hybrid hydrogels. (B) Dried RCA products of polyaptamer template with a 12-mer oligo A sequence or GO-PA hydrogels were placed in water, and swelling ratios were calculated over time. (C) The shear storage modulus, G', and the shear loss modulus, G", of the hydrogels were measured from 0.01 to 10 Hz.
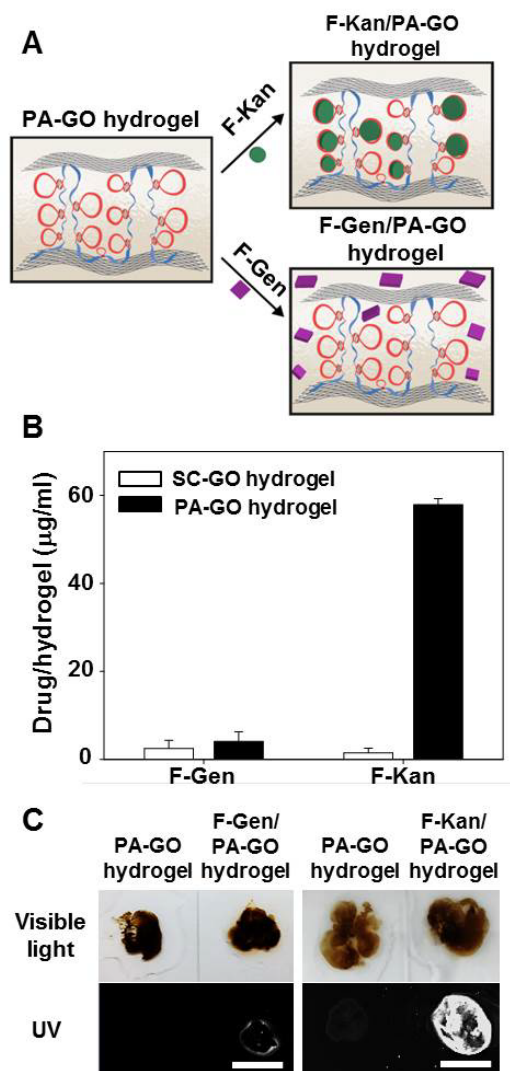
**Fig. IV-4. Drug-specific loading of GO-PA hydrogels.**

(A) Illustration of drug loading into GO-PA hydrogels. (B) F-Kan or F-Gen loading capacity of GO-PA hybrid hydrogels was calculated from the fluorescence of each drug compared to that of the GO-SC hydrogel. (C) Fluorescence images of hydrogels loaded with F-Kan or F-Gen. Scale bars = 1 cm.

## 3.4 Antibacterial effect of Kan/GO-PA hydrogels

Kan/GO-PA exerted significant antibacterial activity against gram-negative *E. coli* (Fig. IV-5A, IV-5B) and gram-positive *S. aureus* (Fig. IV-5A, IV-5C). In contrast, GO-PA showed no significant antibacterial activity against gram-negative (Fig. IV-5A, IV-5B) or gram-positive (Fig. IV-5A, IV-5C) bacteria compared to untreated controls. Survival, measured as colony-forming units (cfu) per plate, was 113.2-fold lower for *E. coli* (Fig. IV-5B) and 94.2-fold lower for *S. aureus* (Fig. IV-5C) in the Kan/GO-PA hydrogel-treated group compared to the untreated group.

## 3.5 GO-PA hydrogel sustainability in vivo

To examine the applicability of the proposed Kan/GO-PA hydrogels, we evaluated their retention at administration sites. To visualize the retention, F-Kan/GO-PA hydrogels were used. For comparison, GO-PA hydrogels were injected in the same amounts and imaged. Following subcutaneous injection, F-Kan/GO-PA hydrogels were retained at the injection site at least for 2 h (Fig. IV-6).
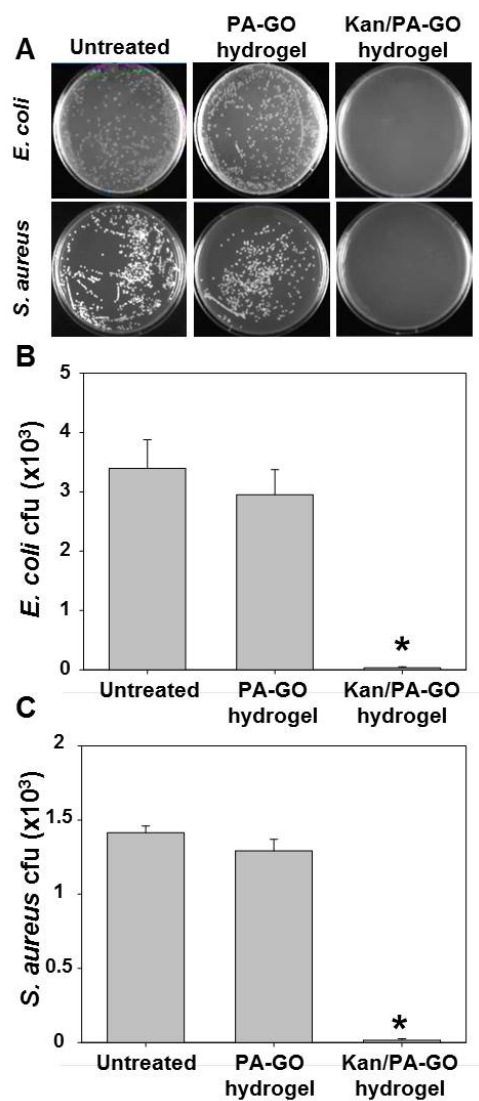
**Fig. IV-5. Antibacterial effects of Kan/GO-PA hybrid hydrogels.**

(A) Colonies of gram-negative *E. coli* and gram-positive *S. aureus* after treatment with GO-PA or Kan/GO-PA hydrogels. The cfu/plate values for *E. coli* (B) and *S. aureus* (C) were determined and expressed as means ± SE (n = 3).

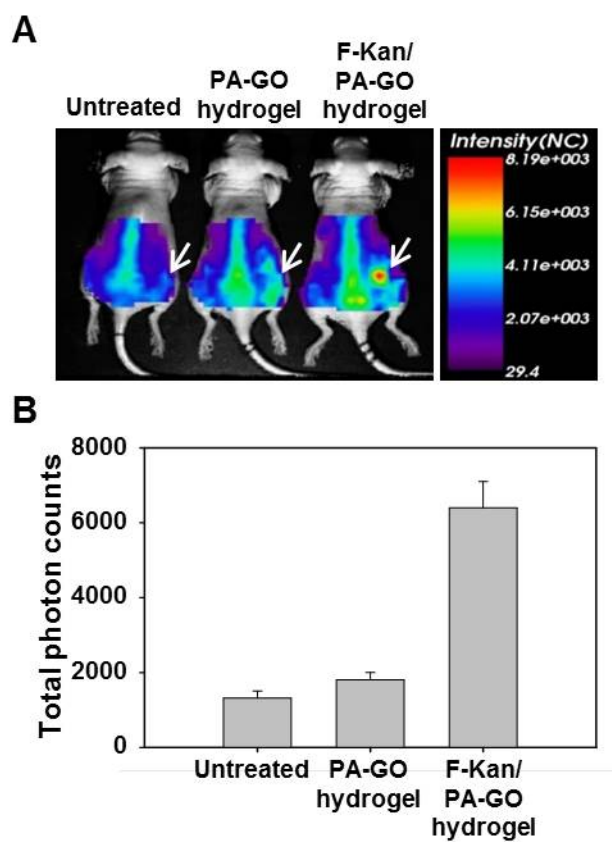**Fig. IV-6.** *In vivo* **retention of hydrogels at injection sites.**

Mice were subcutaneously injected with GO-PA hydrogel or F-Kan/GO-PA hydrogel. The molecular images were obtained immediately after hydrogel injection (A) and 1 h post-injection (B).

## 4. Discussion

Here, we report an injectable GO-PA hybrid hydrogel for use as a drug-delivery system. Drug specificity and loading efficiency were conferred by incorporating a kanamycin-specific DNA aptamer sequence into the RCA template, and GO binding was provided by including a 12-mer oligo A sequence in the RCA template. GO nanosheets acted as a hydrogel crosslinker of RCA products, exploiting the ssDNA-binding property of GO nanosheets. Moreover, Kan/GO-PA hydrogels had rheological properties suitable for an injectable formulation and were retained at the injection site.

GO-PA hybrid hydrogels were generated using a single-step RCA reaction (Fig. IV-1), a reaction made possible by using a 12-mer oligo A as a binder of GO nanosheets. Zhang et al. previously reported that GO nanosheets bind to ssDNA, but not to double-stranded DNA [12]. Lu et al. [16] also reported that GO nanosheets bind fluorescent ssDNA, and quench the fluorescence of ssDNA. But, unlike ssDNA, double-stranded DNA was found to be liberated from GO nanosheets [16]. Given the unique structure-forming ability of aptamer sequences, we expected that the polyaptamer alone might lack sufficient ssDNA regions to bind GO. Indeed, this possibility was supported by our demonstration that RCA products formed using a polyaptamer template without 12-mer oligo A sequences could not form hydrogels in the presence of GO, and instead formed a suspension (Fig. IV-1). Using the single-step RCA reaction to produce hydrogels enabled us to avoid the use of toxic chemical cross-linkers or inconvenient multistep reaction

schemes to produce three-dimensional networks of cross-linked DNA hydrogels.

GO-PA hybrid hydrogels exhibited a bird's nest-like surface morphology with pores (Fig. IV-2). This morphology is similar to that previously reported for RCA-generated DNA hydrogels based on SEM imaging [17]. Given that hydrogels are composed of polymers that crosslink to form a three-dimensional network [18], porosity is an intrinsic property of a hydrogel. Previous studies of DNA-based hydrogel creation methods have used the presence of a porous interior to indicate successful generation of a hydrogel [17,19].

Binding of GO to PA to form hydrogels was further confirmed by XRD patterns (Fig. IV-3A). The $2\theta$ peak for freeze-dried GO that appeared at 9.5° corresponded to a layer-to-layer stacking distance of 8.34 Å [19]. The disappearance of an XRD diffraction peak for freeze-dried GO-PA hydrogels at the same angle could reflect the absence of direct interactions or ordered stacking between GO nanosheets owing to formation of a three-dimensional structure.

GO-PA hybrid hydrogels retained the key characteristics of hydrogels, including swelling and viscoelasticity. Another distinctive feature of GO-PA hydrogels is the 700 % swelling through water absorption (Fig. IV-3B). Compared to previously reported DNA hydrogels, which showed about 100% swelling in 1 day [7], our GO-PA hydrogels showed greater swelling and more rapid swelling kinetics. This superb swelling behavior of GO-PA hydrogels is likely attributable to the dense network of GO-crosslinked hydrophilic DNA components.

In addition to porosity and swelling properties, GO-PA hydrogels were found to exhibit viscoelasticity (Fig. IV-3C). The shear-storage modulus (G') represents the

elasticity of the hydrogel, whereas the shear-loss modulus (G") represents viscosity [20]. Our observation that G' was higher than G" over the entire tested range (0.01 to 10 Hz) indicates that GO-PA formed a solid hydrogel [7]. The values of G' and G" for GO-PA hydrogels fall within the range of injectable hydrogels, regardless of materials used to form the hydrogel [21,22]. Moreover, compared to hydrogels generated with only RCA-produced DNA, which showed a G' less than 10 Pa [17], the elasticity of GO-PA hydrogels was almost 10-fold higher (~100 Pa) in the frequency range of 1 to 10 Hz. These findings imply that the proposed hydrogel platform possesses advantageous mechanical properties, which may be attributable to the presence of the GO crosslinker.

We demonstrated drug-specific loading and high loading efficiency of GO-PA hydrogels using kanamycin as a model drug (Fig. IV-4). The kanamycin-specific loading of GO-PA hydrogels supports the conclusion that GO-PA hydrogels retained the target drug-specific aptamer function. The nucleic acid sequence of the kanamycin-specific aptamer has been previously reported [15]. Although we used kanamycin because of the availability of kanamycin-specific aptamer sequences, the hydrogel system could be used for other antibiotics by replacing aptamer sequences with other antibiotic-specific aptamer sequences. There are reports of DNA aptamers that can recognize and capture other antibiotics, such as tetracycline [23] and gentamicin [24]. Therefore, the application of GO-PA hybrid hydrogel system to other drugs is only limited by the availability of appropriate drug-specific aptamer sequences. Consistent with efficient drug loading, Kan/GO-PA hydrogels exerted antibacterial effects, whereas GO-PA hydrogels did

not (Fig. IV-5). These observations are consistent with recent reports that GO nanosheets alone do not show any antibacterial effects [25-27].

We found that GO-PA hydrogels could be injected through a fine-gauged needle and were retained at the injection site (Fig. IV-6). The retention of hydrogel at the injection site is supported by the viscosity of the gel, as evidenced by rheology data (Fig. IV-3C). Importantly, the injectability of hydrogels, which results from their elastic properties, would enable patients to receive only a bolus injection, thus eliminating the inconvenience of implantation surgery.

# 5. References

[1]    Um SH, Lee JB, Park N, Kwon SY, Umbach CC, Luo D. Enzyme-catalysed assembly of DNA hydrogel. Nat Mat. 2006; 5:797-801.

[2]    Nishikawa M, Ogawa K, Umeki Y, Mohri K, Kawasaki Y, Watanabe H. Injectable, self-gelling, biodegradable, and immunomodulatory DNA hydrogel for antigen delivery. J Control Release. 2014; 180:25-32.

[3]    Costa D, Queiroza J, Miguel MG, Lindman B. Swelling behavior of a new biocompatible plasmid DNA hydrogel. Colloid Surface B. 2012; 92: 106-112.

[4]    Baeissa A, Dave N, Smith BD, Liu J. DNA-functionalized monolithic hydrogels and gold nanoparticles for colorimetric DNA detection. ACS Appl Mater Inter. 2010; 2:3594-3600.

[5]    Zhu Z, Wu C, Liu H, Zou Y, Zhang X, Kang H. An aptamer cross-linked hydrogel as a colorimetric platform for visual detection. Angew Chem Int Edit. 2010; 49:1052-1056.

[6]    Topuz F, Okay O. Formation of hydrogels by simultaneous denaturation and cross-linking of DNA. Biomacromolecules. 2009; 10:2652-2661.

[7]    Karacan P, Cakmak H, Okay O. Swelling behavior of physical and chemical DNA hydrogels. J Appl Polym Sci. 2012; 128:3330-3337.

[8] Kang H, Liu H, Zhang X, Yan J, Zhu Z, Peng L. Photoresponsive DNA-cross-linked hydrogels for controllable release and cancer therapy. Langmuir. 2011; 27: 399-408.

[9] Xing Y, Cheng E, Yang Y, Chen P, Zhang T, Sun Y. Self-assembled DNA hydrogels with designable thermal and enzymatic responsiveness. Adv Mater. 2011; 23:1117-1121.

[10] Nöll T, Schönherr H, Wesner D, Schopferer M, Paululat T, Nöll G. Construction of three-dimensional DNA hydrogels from linear building blocks. Angew Chem Int Edit. 2014; 53: 1-6.

[11] Nishikawa M, Mizuno Y, Mohri K, Matsuoka N, Rattanakiat S, Takahashi Y. Biodegradable CpG DNA hydrogels for sustained delivery of doxorubicin and immunostimulatory signals in tumor-bearing mice. Biomaterials. 2011; 32: 488-494.

[12] Zhang H, Jia S, Lv M, Shi J, Zuo X, Su S. Size-dependent programming of the dynamic range of graphene oxide-DNA interaction-based ion sensors. Anal Chem. 2014; 86:4047-4051.

[13] Kim MG, Shon Y, Lee J, Byun Y., Choi BS, Kim YB, Oh YK. Double stranded aptamer-anchored reduced graphene oxide as target-specific nano detector. Biomaterials. 2014;35: 2999-3004.

[14] Miao W, Shim G, Lee S, Lee S, Choe YS, Oh YK. Safety and tumor tissue

accumulation of pegylated graphene oxide nanosheets for co-delivery of anticancer drug and photosensitizer. Biomaterials. 2013; 34:3402-3410.

[15] Song KM, Cho M, Jo H, Min K, Jeon SH, Kim T. Gold nanoparticle-based colorimetric detection of kanamycin using a DNA aptamer. Anal Biochem. 2011; 415:175-181.

[16] Lu CH, Yang HH, Zhu CL, Chen X, Chen GN. A graphene platform for sensing biomolecules. Angew Chem. Int Edit. 2009; 48: 4785-4787.

[17] Lee JB, Peng S, Yang D, Roh YH, Funabashi H, Park N. A mechanical metamaterial made from a DNA hydrogel. Nat Nanotechnol. 2012; 7:816-820.

[18] Satarkar NS, Biswal D, Hilt JZ. Hydrogel nanocomposites: a review of applications as remote controlled biomaterials. Soft Matter. 2010; 6:2364-2371.

[19] Xu Y, Wu Q, Sun Y, Bai H, Shi G. Three-dimensional self-assembly of graphene oxide and DNA into multifunctional hydrogels. ACS Nano. 2010; 4:7358-7362.

[20] Yan C, Pochan DJ. Rheological properties of peptide-based hydrogels for biomedical and other application. Chem Soc Rev. 2010; 39:3528-3540.

[21] Tan H, Ramirez CM, Miljkovic N, Li H, Rubin JP, Marra KG. Thermosensitive injectable hyaluronic acid hydrogel for adipose tissue

engineering. Biomaterials. 2009; 30:6844-6853.

[22] Feng S, Chen H, Liu Y, Huang Z, Sun X, Zhou L. A novel vitreous substitute of using a foldable capsular vitreous body injected with polyvinylalcohol hydrogel. Sci Rep. 2013; 3:1838.

[23] Niazi JH, Lee SJ, Gu MN. Single-stranded DNA aptamers specific for antibiotics tetracyclines. Bioorgan Med Chem. 2008; 16: 7245-7253.

[24] Rowe AA, Miller EA, Plaxco KW. Reagentless measurement of aminoglycoside antibiotics in blood serum via an electrochemical, **r**ibonucleic acid aptamer-based biosensor. Anal Chem. 2010; 82: 7090-7095.

[25] Park S, Mohanty N, Suk JW, Nagaraja A, An J, Piner RD. Biocompatible, robust free-standing paper composed of a TWEEN/graphene composite. Adv Mater. 2010; 22:1736-1740.

[26] Das MR, Sarma RK, Saikia R, Kale VS, Shelke MV, Sengupta P. Synthesis of silver nanoparticles in an aqueous suspension of graphene oxide sheets and its antimicrobial activity. Colloid Surface B. 2011; 83:16-22.

[27] Ruiz ON, Fernando KA, Wang B, Brown NA, Luo PG, McNamara ND. Graphene oxide: a nonspecific enhancer of cellular growth. ACS Nano. 2011; 5:8100-8107.

## Conclusion

Rolling circle amplification (RCA) is an isothermal, enzymatic process mediated by unique DNA and RNA polymerases in which long single-stranded (ss) DNA molecules are produced on a short circular ssDNA template by using a single DNA primer. As RCA products contain repetitive sequences that are complementary to the circular DNA template, the DNA products can be manipulated to include multifunctional sequences by designing the DNA template. These functional RCA-based nanotechnologies have been utilized for various biomedical applications including drug delivery.

For delivery of antisense oligonucleotides (ASOs), we developed biomimetic hyaluronic acid (HA)-coated, Mu peptide-condensed, dual ASO-loaded DNA nanoballs (HMA nanoballs). RCA technique was used for amplification of ASO-binding sequences, and dual ASOs, Dz13 and OGX-427, were incorporated onto HMA nanoballs through sequence-specific complementary hybridization. Surface coating with HA enhanced CD44 receptor-mediated delivery of HMA nanoballs to tumor cells. Importantly, ASOs delivered by HMA nanoballs suppressed the expression of their target mRNAs of ASO, exerting potent anticancer effects in vitro and in vivo upon co-treatment with doxorubicin (Dox).

Although DNA aptamers have emerged as a potential targeting moiety for drug delivery systems, their binding affinity is generally lower than that of antibodies. To overcome the problem, we synthesized tumor cell-specific polyaptamer nanothreads by RCA. Reduced graphene oxide (rGO) coated with protein tyrosine

kinase 7 (PTK7) polyaptamer nanothreads (PNTrGO) improved cellular uptake into PTK7-positive tumor cells lines and enhanced tumor tissue accumulation compared to scrambled polyaptamer-anchored rGO nanosheets. Moreover, systemic administration of Dox using PNTrGO enhanced the antitumor effects in mice bearing PTK7-positive tumors.

Graphene oxide-crosslinked DNA polyaptamer (GO-PA) hybrid hydrogels were constructed by running single RCA of DNA template in the presence of GO nanosheet. PA-GO hybrid hydrogels exhibited a bird's nest-like surface morphology, a swelling ratio of 657% at 2 h, and viscoelasticity suitable for injection and retention. PA-GO hybrid hydrogels specifically bound Kan, exhibiting a drug loading efficiency of 58.0% for Kan compared with 1.5% for gentamicin. Kan-loaded PA-GO (Kan/PA-GO) hybrid hydrogels exerted antibacterial activity against gram-negative (*Escherichia coli*) and gram-positive (*Staphylococcus aureus*) bacteria. In mice, subcutaneously injected, fluorescent Kan-loaded PA-GO hybrid hydrogel was retained at the injection site.

In our proof-of-principle study, functional DNA nanostructure by RCA technique has been developed. The RCA-based DNA nanostructures were capable of delivery of gene, chemical drug, and antibiotics. Overall, these DNA nanostructure-based systems are promising for various drug deliveries.

# 요약

# DNA 나노구조 기반 약물 전달 연구

서울대학교 대학원

약학과 약제과학전공

김미경

Rolling circle amplification(RCA)을 활용한 나노 전달체 제조기술은 약물전달 분야에서 신규한 전달체를 개발하기 위한 차세대 기술로서 각광받고 있다. RCA 반응으로 제조한 DNA nanoball은 antisense oligonucleotide(ASO)의 상보적인 서열을 포함하므로 두 가지 이상의 ASO(Dz13, OGX-427) 의약을 서열 특이적으로 탑재 가능하다. 또한, DNA nanoball의 표면에 코팅된 히알루론산에 의해 암세포조직에 과발현하는 CD44수용체에 특이적으로 ASO 의약을 전달할 수 있다. DNA nanoball에 의해 세포 내로 전달된 ASO는 타겟 mRNA(HSP27, c-jun)의 발현을 억제하여 세포와 소동물 수준에서 강력한 항암효과를 보였다.

RCA 기술을 활용하여 단백질 인산화 효소로 알려진 protein tyrosine

kinase 7(PTK7)에 특이적으로 결합 가능한 DNA polyaptamer nanothread를 합성하였다. DNA polyaptamer nanothread를 합성할 때 사용되는 DNA template에는 bridge 서열을 포함시켜 환원 그래핀 나노시트(rGO)와의 interaction을 향상시키고자 하였다. 합성된 DNA polyaptamer nanothread를 환원그래핀 나노시트(PNTrGO)의 표면에 부착한 결과, 표적능이 없는 DNA polyaptamer nanothread을 부착한 환원그래핀 나노시트(SNTrGO)와 비교하였을 때, 표적 PTK7 단백질이 과발현하는 암 세포주 및 암 조직에서 향상된 세포전달능력 및 축적능력을 확인하였다. 더 나아가 항암의약 독소루비신(doxorubicin)을 탑재한 후 표적 PTK7 단백질을 과발현하는 암 동물모델에 전신투여 하였을 때 항암효과가 있음을 확인하였다.

항생제 약물에 특이적으로 결합 가능한 DNA polyaptamer를 RCA반응으로 제조하고 여기에 crosslinker 역할을 할 수 있는 그래핀 나노시트를 첨가하여 주입형 하이드로겔을 개발하였다. GO-PA 하이브리드 하이드로겔은 특이적으로 항생제 카나마이신을 탑재할 수 있다. GO-PA 하이브리드 하이드로겔에 카나마이신과 젠타마이신을 탑재하여 약물 특이적 loading 효율을 비교한 결과, 카나마이신은 58.0%, 젠타마이신은 1.2%의 탑재효율을 보였다.

주요어: DNA nanoball, rolling circle replication, drug delivery, aptamer, graphene nanosheet, reduced graphene nanosheet

학 번: 2011-30500